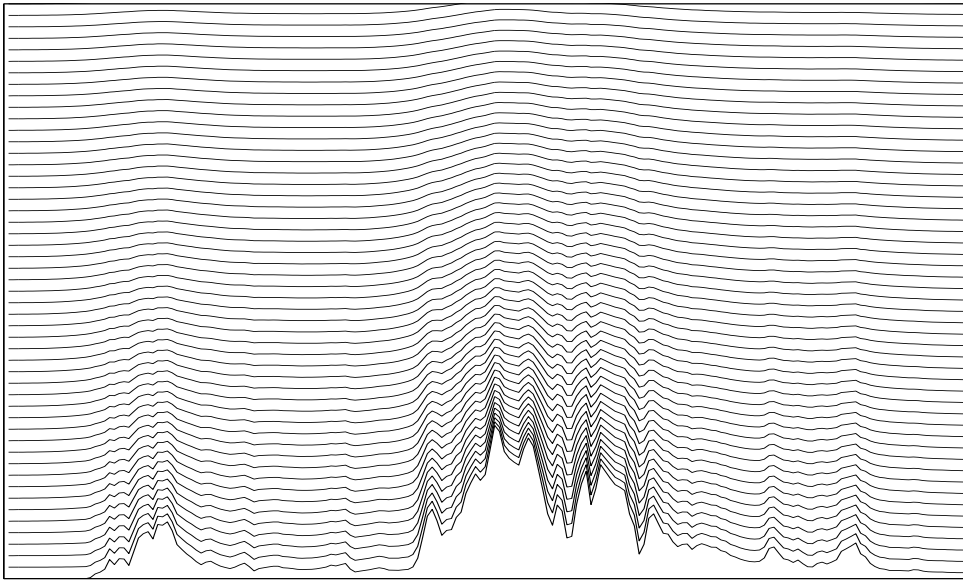


A New Terrain-Following Coordinate for High-Resolution Atmospheric Models



Diploma Thesis

Daniel Leuenberger

Thesis Supervisors

Prof. Dr. Ch. Schär, Climate Research ETH, Zürich

Oliver Fuhrer, Climate Research ETH, Zürich

Dr. D. Lüthi, Atmospheric Science ETH, Zürich

ETH Zürich, Computational Science and Engineering

March 2001

Title figure

Level-heights of the new, scale-dependent terrain-following coordinate presented in this study. The topography corresponds to a south-north cross-section of an unfiltered MC2 model topography of the Alps with a resolution of 3 km . Geographical locations on this cross-section are (from left to right): Gulf of Genova, Po valley, Aosta valley, Monte Rosa massif, Valais, Bernese Alps, Lake of Thun, Emmental region. The horizontal and vertical extents of the domain are 600 km and 15 km respectively.

Corresponding author address

Daniel Leuenberger

Beckhammer 3

CH-8057 Zürich

leuenberger@geo.umnw.ethz.ch

Contents

Contents	i
Acknowledgements	iii
Abstract	v
1 Introduction	1
2 A New Generalized Vertical Coordinate	3
2.1 Introduction to Terrain-Following Coordinates	3
2.2 Definition of the New Coordinate	5
2.3 Metric terms	6
2.4 Invertibility Condition	7
3 An idealized 2D Advection Study	9
3.1 Description of the Model	9
3.2 Experiments	11
3.3 Results	12
4 Application in a High-Resolution Atmospheric Model	15
4.1 The MC2 Model	15
4.2 Implementation of the New Coordinate into MC2	17
4.2.1 Splitting of the Topography	17
4.2.2 Treatment of the Metric Terms	18
4.3 Idealized Case Studies	22
4.3.1 Case study 1: Stagnant Layer over 3D-Topography	22
4.3.2 Case study 2: Uniform Flow past Complex 2D-Topography	32
5 Conclusion and Outlook	41
References	46
Nomenclature	47
A Selected Experiment Results	49
A.1 Case study 2, Experiment 2	49
A.2 Case study 2, Experiment 4	52

Acknowledgements

During the time of writing my diploma thesis I could rely on many helping friends and colleagues, without whom this thesis would not have been possible. I greatly enjoyed the time spent in the friendly and uncomplicated atmosphere of the Institute of Climate Research, ETH Zürich!

- Above all I am deeply grateful to *Oliver Fuhrer*. He always had an open office, was never tired to patiently answer my endless questions and guided me safely and professionally through the jungle of the thousands of MC2 shell-scripts. I really learned a lot from his optimism and his efficient way of solving problems. He also reviewed this text with a major effort and showed deep interest in this work. Thanks for the great time!
- A big thanks to *Prof. Christoph Schär* who gave me the opportunity to work in the highly interesting field of numerical atmospheric modelling. He repeatedly supported the first 'stranger' from Rechnergestützte Wissenschaften and enabled me to participate in several interesting projects.
- I would like to express my gratitude to *Daniel Lüthi* from Atmospheric Science ETH for his assistance concerning the MC2 code.
- Thanks to *Claude Girard* from Recherche en Prévision Numérique (RPN), Environment Canada, Dorval and to *Daniel Lüthi* for the preparation of parts of the MC2 code.
- Thanks also to all members of the Institute of Climate Research who contributed to the friendly and warm atmosphere and answered many questions concerning \LaTeX and MC2 features, namely to *Jürg Schmidli*, *André Walser*, *Reto Stöckli*, *Sonia Seneviratne*, *Chrigel Frei*, *Karsten Jasper* and *Jan Kleinn*.
- A huge thanks goes to *Petra* for her love and support and for letting me know, that there are other things in life than coordinate transformations . . .
- I'm deeply indebted to my parents, who always make me feel at home and generously and trustfully supported all my plans during the past years.
- And finally a big thanks to my brother *Adrian* and all my friends who cannot be listed here for sharing great moments. You know who you are!

Abstract

In recent development of numerical weather prediction (NWP) models there is a trend towards high-resolution non-hydrostatic models with horizontal grid intervals of just a few kilometers. When modelling regions with complex terrain, like the Alps, fine-scale features appear in the model topography with wavelengths less than 10 grid intervals. These features also appear in the computational level-heights of a terrain-following vertical coordinate and may introduce considerable errors in the simulation. Since the upper-level atmospheric flow is often decoupled from near-surface flow, it need not follow the small-scale features of the topography. Therefore it is an important issue to choose an appropriate coordinate transformation, which is well suited for the flow features to be simulated. Experience has shown that it is desirable for the coordinate transformation to form smooth level-heights in upper regions of the domain.

In this study, a new, terrain-following vertical coordinate is successfully implemented in a non-hydrostatic NWP model and tested with idealized flow simulations involving two different flow profiles and topographies of various complexity. The coordinate has a scale-dependent vertical decay of the terrain-features and allows for a fast and smooth transition from terrain-following to horizontal computational levels. Results are compared with those obtained with other vertical coordinates, namely with the *Gal-Chen* coordinate and a hybrid-like coordinate.

We show, that both the hybrid and the new coordinate exhibit a clearly improved performance as compared to the *Gal-Chen* coordinate in representing horizontal flow features over complex topography. The difference in the performance of the coordinates is observed to be less distinct, if the flow features the same horizontal scale as the structure of the underlying topography, as is the case for pure hydrostatic mountain waves. However, if flows featuring both small-scale hydrostatic and large-scale non-hydrostatic waves are simulated, the *Gal-Chen* coordinate fails to accurately reproduce the large-scale structures of the wave. Moreover, the results obtained with the new coordinate are not only superior to those of the *Gal-Chen* coordinate but also to those of the hybrid-like coordinate, which demonstrates the advantage of a scale-dependent vertical decay of the terrain features.

Zusammenfassung

Der Trend der aktuellen Entwicklung von numerischen Wettervorhersagemodellen geht immer mehr in Richtung hochauflösender, nichthydrostatischer Modelle mit horizontalen Gitterabständen von wenigen Kilometern. Die Simulation von Gebieten mit extremer Topographie, wie z.B. die Alpen, führt dazu, dass die Modelltopographie feinskalige Strukturen mit Wellenlängen von weniger als 10 Gitterpunkten aufweisen kann. Diese Strukturen werden auch in die Höhen der Modellflächen von geländefolgenden vertikalen Koordinaten übernommen und können erhebliche numerische Fehlerquellen darstellen. Da atmosphärische Strömungen in der Höhe vielfach von denen entlang des Bodens entkoppelt sind und den feinskaligen Strukturen der Topographie nicht folgen, kommt der Wahl einer geeigneten vertikalen Koordinatentransformation entscheidende Bedeutung zu. Erfahrungen haben gezeigt, dass es von Vorteil ist, wenn die Koordinatentransformation in höheren Lagen glatte Modellflächen erzeugt.

Diese Arbeit beinhaltet die erfolgreiche Implementation und den Test einer neuen vertikalen Koordinate für ein nichthydrostatisches numerisches Wettermodell. Idealisierte Simulationen mit zwei verschiedenen Geschwindigkeitsprofilen und verschieden komplexer Topographie wurden durchgeführt. Die neue Koordinate hat einen skalenabhängigen vertikalen Zerfall der Terrainstrukturen und erlaubt einen raschen und glatten Übergang von geländefolgenden zu horizontalen Modellflächen. Zum Vergleich wurden auch Simulationen mit der *Gal-Chen*-Koordinate und einer hybrid-ähnlichen Koordinate durchgeführt.

Es wird gezeigt, dass sowohl mit der Hybridkoordinate, als auch mit der neuen Koordinate für die Berechnung von horizontalen Strömungen über komplexen Gebirgen deutlich bessere Ergebnisse erzielt werden, als mit der *Gal-Chen*-Koordinate. Der Unterschied zwischen den verschiedenen Koordinaten ist weniger ausgeprägt, wenn die Strömung ähnliche horizontale Skalen aufweist, wie die des unterliegenden Gebirges, so zum Beispiel für reine hydrostatische Schwerewellen. Wenn jedoch Strömungen simuliert werden, in denen sowohl grobskalige hydrostatische und feinskalige nicht-hydrostatische Wellen angeregt werden, ist die *Gal-Chen*-Koordinate nicht in der Lage, die grobskaligen Strukturen der Wellen richtig wiederzugeben. Ergebnisse zeigen, dass die neue Koordinate nicht nur der *Gal-Chen*-Koordinate, sondern auch der hybrid-ähnlichen Koordinate überlegen ist und demonstrieren klar den Vorteil von skalenabhängigem vertikalem Zerfall von Geländestrukturen in der Koordinatentransformation.

Chapter 1

Introduction

In physical and mathematical modelling the choice of the coordinates in which the governing equations are expressed can be of great importance for mainly three reasons: Firstly, an equation's form can be simplified drastically if written in an appropriate coordinate system, allowing the application of simpler and more accurate solving techniques. Secondly, the treatment of irregular boundaries can be facilitated significantly by choosing suitable coordinates. Thirdly, computational errors caused by the coordinate transformation can be reduced, if an appropriate formulation is chosen.

In atmospheric modelling special attention has been paid to the vertical coordinate because of the characteristic vertical structure and aspect ratio of the atmosphere and its irregular lower boundary.

Non-Terrain-Following coordinates

The most natural choice is the use of the height z or the radial distance r from the center of the earth as a vertical coordinate. It is everywhere orthogonal to the horizontal (x, y) -plane in the Cartesian framework or to the (λ, φ) -plane in spherical coordinates. The application of standard difference techniques is easy and if there is no topography the treatment of the boundary conditions is straightforward.

In hydrostatic models the pressure in hydrostatic equilibrium p is often used as a vertical coordinate. In hydrostatic equilibrium, p is a monotone function of height and this choice is feasible. The main advantages of the p -coordinate over z are that the continuity equation and the pressure force in the horizontal momentum equations become linear in this frame of reference.

Isentropic surfaces, or equivalently, potential temperature θ -surfaces can be used as a vertical coordinate for the simulation of dry flow and if the atmosphere is stably stratified, i.e. $\frac{\partial \theta}{\partial z} > 0$. θ -coordinates have the attractive property that dry adiabatic processes are two-dimensional, since θ is conserved along the motion. They also give a better resolution in the vicinity of fronts. However, since the atmosphere is not always and everywhere stably stratified, θ is not necessarily a monotonic function of the height and cannot always be used.

Terrain-Following coordinates

If the lower boundary of the considered domain is not flat, the vertical coordinates described above all have the serious disadvantage, that isosurfaces of the vertical coordinate may intersect with the topography. Thus, if structured meshes are employed, the posing of boundary conditions (like no flow across the rigid surface) can become a painful task. This problem can be avoided by the use of a terrain-following vertical coordinate, where the domain with irregular boundary is mapped to a rectangular domain.

In hydrostatic models a normalized pressure coordinate $\sigma = p/p_s$ (Phillips, 1957) is widely-used. p_s denotes the surface pressure and σ ranges from zero at the top of the physical domain to one at the surface. The mentioned lower boundary condition can easily be posed by setting the vertical σ -velocity $\frac{D\sigma}{Dt} = 0$ at the surface and the top of the domain. A disadvantage of the σ -coordinate arises over steep topography, where transformational and numerical errors lead to inaccurate calculation of the horizontal pressure gradient.

For non-hydrostatic models the choice of pressure as a vertical coordinate does not have substantial advantages. Current mesoscale models often apply a terrain-following coordinate proposed by Gal-Chen and Somerville (1975) or hybrid derivations based on the idea of Simmons and Burridge (1981). Experience has shown, however, that simulated flow fields with these coordinates can feature fine-scale patterns above complex topography, which are unlikely to be of physical origin. It is believed, that these errors are partly produced by the numerical transformation of the vertical coordinate and that they can cause significant changes in the vertical velocity and in the predicted precipitation fields.

Since upper-level flow is often decoupled from the near-surface flow, it is not desirable for upper computational level-heights to feature topographic structure, as is the case for near-surface level-heights. Schär (2000a) therefore proposed a new vertical coordinate based on a non-local transformation, which allows for a fast transition from terrain-following to horizontal level-heights by the use of a scale-dependent vertical decay of topographic features. In a simple numerical advection test, this formulation has proven to be superior to that of the Gal-Chen coordinate. (Schär, 2000b)

This study aims at the investigation of the behaviour of the new coordinate mentioned above in a non-hydrostatic numerical weather prediction model employing full dynamics and complex topography. For this purpose, idealized simulations of atmospheric flow employing two different flow profiles and topographies of various complexity are performed. The performance of the new coordinate is compared with that of the Gal-Chen coordinate and a hybrid coordinate.

The remainder of this report is structured as follows: In the first chapter, some theoretical aspects of the new vertical coordinate are captured. In a second chapter, a sensitivity study the investigates the performance of the new coordinate in a simple numerical test involving horizontal advection over complex topography. The main part of the study focuses on implementation topics and presents idealized simulations with the non-hydrostatic model. Due to the limited scope of this work, only the dynamics of the model is tested and physical parametrizations are not included.

Chapter 2

A New Generalized Vertical Coordinate

2.1 Introduction to Terrain-Following Coordinates

In most of the interesting real-case applications the physical domain has boundaries, which are far away from being plane. If standard differencing with structured grids is used to discretize the governing equations, the treatment of appropriate boundary conditions like no flow through the rigid surface can be significantly simplified, if the irregular domain is transformed to a rectangular domain.

In atmospheric modelling, particularly when treating mesoscale phenomena with high-resolution models, the topography can have significant influence on the dynamics and the thermodynamics of the flow. Therefore, it is of great importance to accurately include topography in the model. In the remainder of this section a brief overview of terrain-following vertical coordinate transformations is given.

A general vertical coordinate transformation can be defined by

$$\eta = \eta(x, y, z) \quad (2.1)$$

where x, y, z are the cartesian coordinates of the physical domain

$$x_{min} \leq x \leq x_{max}, \quad y_{min} \leq y \leq y_{max}, \quad 0 \leq h(x, y) \leq z \leq H \quad (2.2)$$

$h(x, y)$ and H denote the topography and the height of the upper lid of the model, respectively. For a terrain-following coordinate transformation [Gal-Chen and Somerville \(1975\)](#) mainly proposed the following requirements:

- I The domain (2.2) is to be transformed into a rectangular domain
- II The transformation shall be invertible. (2.3)
- III If the topography is flat, the transformation shall be the Identity transformation.

Requirement I is met by imposing the boundary conditions

$$\eta(x, y, h) = 0 \quad (2.4a)$$

on the Earth's surface $z = h(x, y)$ and

$$\eta(x, y, H) = H \quad (2.4b)$$

at the upper lid $z = H$. The computational domain

$$x_{min} \leq x \leq x_{max}, \quad y_{min} \leq y \leq y_{max}, \quad 0 \leq \eta \leq H \quad (2.5)$$

is then spanned by the coordinates x, y, η and surfaces of constant η follow the topography at the bottom, while they become horizontal at the model lid H .

Requirement II is satisfied, if there exists an inverse transformation

$$z = z(x, y, \eta) \quad (2.6)$$

to (2.1). In the case, where just the vertical coordinate is transformed, it is sufficient to require the function $\eta(x, y, z)$ to be monotonic throughout the whole domain, i.e. $J = \frac{\partial \eta}{\partial z} > 0$. Here J denotes the determinant of the Jacobian matrix of the transformation, furtheron called Jacobian. The importance of this invertibility condition will be treated in Section 2.4.

The transformation proposed by [Gal-Chen and Somerville \(1975\)](#) takes the form

$$\eta(x, y, z) = H \frac{z - h(x, y)}{H - h(x, y)} \quad (2.7)$$

and satisfies all conditions listed above. In particular the invertibility condition is satisfied and the inverse transformation writes

$$z(x, y, \eta) = \eta + h(x, y) \frac{H - \eta}{H}. \quad (2.8)$$

Note, that with this coordinate the terrain features decay linearly with height. Many non-hydrostatic Numerical Weather Prediction (NWP) models therefore use hybrid coordinates following the study of [Simmons and Burridge \(1981\)](#). Their formulation was originally intended for pressure coordinates, but it can also be applied to z -coordinates. The idea is to choose terrain-following coordinates in the lower part of the domain and simple z -coordinates in the upper part. Such a coordinate transformation can be defined as

$$z(x, y, \eta) = a(\eta) + h(x, y)b(\eta), \quad (2.9)$$

where $a(\eta)$ defines the height of the level η in absence of topography and the decay function $b(\eta)$ governs the vertical decay of the topography signal. To be consistent with the requirements (2.3) the functions $a(\eta)$ and $b(\eta)$ must satisfy the following conditions:

$$a(0) = 0, \quad a(H) = H, \quad b(0) = 1, \quad b(H) = 0 \quad (2.10)$$

The definition of $a(\eta)$ and $b(\eta)$ is usually done in a numerical table and easily allows for unequally spaced computational surfaces, which can be of advantage to accurately resolve the planetary boundary layer. However, following this approach, the computational levels are also unequally spaced, which can reduce the order of accuracy of the vertical spacial discretization. It is more efficient to set

$$a(\eta) = \eta, \quad (2.11)$$

to add a second analytic transformation $Z = Z(\eta)$ and to discretize the governing equations in the Z -space based on constant ΔZ increments. With this approach the order of accuracy of the vertical discretization has no limitations due to an unequal spacing of the levels in the computational space. [Figure 2.1](#) shows the height of the computational levels in the three frames of reference. In the remaining part of this and the next chapter, we will focus on the transformation to η -coordinates with equally spaced levels. In [Chapter 4](#) the second transformation will be included and thus, we will refer to the Z -space as the computational space.

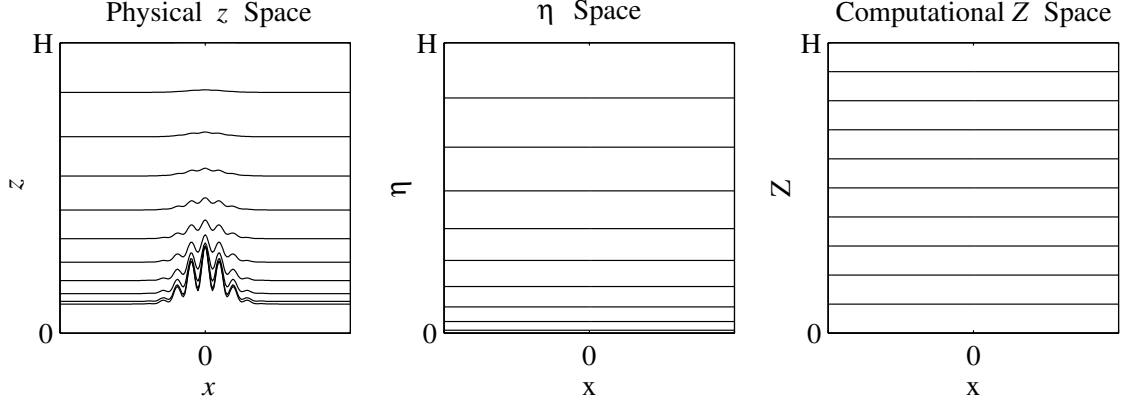


Figure 2.1: Height of the computational levels in Physical z -coordinates (left), η -coordinates (middle) and computational Z -coordinates (right).

Vertical decay functions

The decay with height of the topography $h(x, y)$ is governed by the vertical decay function $b(\eta)$, which must be chosen in a way, that Eq. (2.9) satisfies the boundary conditions (2.10) and the invertibility condition, but otherwise, it can be arbitrarily chosen. The *Gal-Chen* coordinate (2.8) can be interpreted as a special case of the *Simmons and Burridge* formulation with

$$b(\eta) = \frac{H - \eta}{H}$$

Note, that underlying topography features decay linearly with height and the Jacobian does not decay but is constant with height. This can be considered as a drawback of the *Gal-Chen* coordinate, since the terrain-induced features in upper-level computational surfaces may cause considerable numerical error in the calculation of quasi-horizontal phenomena.

The use of a simple version of hybrid coordinates partly avoids this problem. Terrain features are included in the coordinate only below a level H_1 , where above this level simple z -coordinates are used. A common formulation is

$$b(\eta) = \begin{cases} \frac{H_1 - \eta}{H_1} & : 0 \leq \eta \leq H_1 \\ 0 & : H_1 < \eta \leq H \end{cases} \quad (2.12)$$

At $\eta = H_1$ the Jacobian-determinant of the transformation, and thus, all other metric terms, are not defined, which might cause an inaccurate transformation of the governing equations.

[Schär \(2000a\)](#) proposed a decay function, which leads to an exponential decay of the underlying terrain features:

$$b(\eta) = \frac{\sinh((H - \eta)/s)}{\sinh(H/s)} \quad (2.13)$$

The rate of decay is governed by the single parameter s which can be considered as a scale height i.e. the terrain features decay by a factor of $1/e$ over a vertical distance s . By setting $s \approx H$, a *Gal-Chen* like formulation is obtained, while for $s < H$ the structure is comparable to that of a hybrid coordinate. The coordinate transformation defined by Eq. (2.9), (2.11) and (2.13) is hereafter referred to as 'exponential coordinate'. Figure 2.2 shows a plot of the decay functions described above.

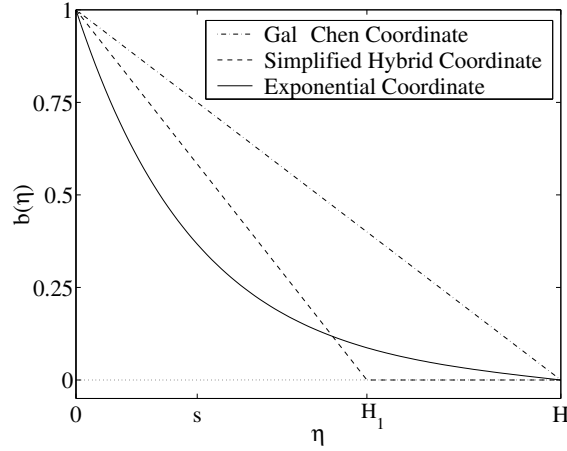


Figure 2.2: Comparison of the vertical decay functions $b(\eta)$ of the Gal-Chen coordinate Eq. (2.8) (dash-dotted line), a hybrid coordinate Eq. (2.12) (dashed line) and an exponential coordinate Eq. (2.13) with scale height $s = H/4$ (solid line)

2.2 Definition of the New Coordinate

All the formulations described above have the common property, that the coordinate transformation is local and depends on the height of the topography alone. Therefore any terrain feature is damped with the same rate, irrespective of its height and shape. Since the upper-level atmospheric flow is often decoupled from the near-surface flow, the computational levels need not follow the terrain shape in higher regions of the domain. Schär (2000a) proposed a new formulation, which takes this into account and makes better use of the generality of (2.1). The idea is to apply a scale-dependent vertical decay of the terrain, which allows for a rapid decay of the small-scale features and thus for a fast transition to smooth levels-heights. The height of the computational levels is therefore dependent on the shape of the terrain and thus the transformation is referred to as non-local.

The topography $h(x, y)$ is split into a large-scale part $h_1(x, y)$ and a small-scale part $h_2(x, y)$ satisfying

$$h(x, y) = h_1(x, y) + h_2(x, y). \quad (2.14)$$

In practice this will be done by the application of a smoothing digital filter. The two parts of the topography decay exponentially with separate scale-heights s_1 and s_2 , referring to the large-scale and small-scale part of the topography, respectively. The definition of the new coordinate reads

$$z(x, y, \eta) = \eta + h_1(x, y)b_1(\eta) + h_2(x, y)b_2(\eta) \quad (2.15)$$

with the vertical decay functions

$$b_i(\eta) = \frac{\sinh((H - \eta)/s_i)}{\sinh(H/s_i)}, \quad i = 1, 2. \quad (2.16)$$

This coordinate transformation is hereafter referred to as 'new coordinate'.

2.3 Metric terms

The governing equations of a model are usually derived in the cartesian frame of reference. In order to benefit from the simplifications of the equations when formulated in another coordinate

system, they need to be transformed to and solved in the new system. Since the laws of physics do not depend on the coordinate system, any scalar variable A may be expressed in terms of either the cartesian coordinate or any other coordinate system, i.e. $A(x, y, z, t)$ or $A(x, y, \eta, t)$. If A is transformed from z -coordinates to η -coordinates $A(x, y, z, t)$ has to be replaced by $A(x, y, \eta, t) \equiv A(x, y, z(x, y, \eta), t)$. Partial derivatives with respect to r , where r stands for one of x, y, t , are transformed according to the expression

$$\left(\frac{\partial A}{\partial r}\right)_\eta = \left(\frac{\partial A}{\partial r}\right)_z + \frac{\partial A}{\partial z} \left(\frac{\partial z}{\partial r}\right)_\eta \quad (2.17a)$$

where the subscript denotes the variable held constant when taking the derivative. Similarly, the vertical derivatives are related as follows:

$$\frac{\partial A}{\partial \eta} = \frac{\partial A}{\partial z} \frac{\partial z}{\partial \eta}, \quad \text{resp.} \quad \frac{\partial A}{\partial z} = \frac{\partial A}{\partial \eta} \frac{\partial \eta}{\partial z} \quad (2.17b)$$

The relations (2.17) can be used to determine the metric terms which will appear in the transformed equations. In practice, the following terms will usually be needed:

$$\frac{\partial z}{\partial \eta}, \quad \left(\frac{\partial \eta}{\partial x}\right)_z, \quad \left(\frac{\partial \eta}{\partial y}\right)_z \quad (2.18)$$

which may be computed from (2.15) as

$$\frac{\partial z}{\partial \eta} = 1 + h_1(x, y) \frac{\partial b_1}{\partial \eta} + h_2(x, y) \frac{\partial b_2}{\partial \eta} \quad (2.19a)$$

$$\left(\frac{\partial z}{\partial x}\right)_\eta = \frac{\partial h_1}{\partial x} b_1 + \frac{\partial h_2}{\partial x} b_2 \quad (2.19b)$$

$$\left(\frac{\partial z}{\partial y}\right)_\eta = \frac{\partial h_1}{\partial y} b_1 + \frac{\partial h_2}{\partial y} b_2 \quad (2.19c)$$

where

$$b_i(\eta) = \frac{\sin((H - \eta)/s_i)}{\sinh(H/s_i)} \quad \text{and} \quad \frac{\partial b_i}{\partial \eta} = \frac{-\cosh((H - \eta)/s_i)}{s_i \sinh(H/s_i)} \quad i = 1, 2$$

The implementation of the metric terms in the code can either be done by using the expressions (2.19), which can be evaluated analytically except of the horizontal derivatives of the topography, or by approximating (2.18) with finite differences on the computational grid.

2.4 Invertibility Condition

As mentioned in Section 2.1, a coordinate transformation must have a unique inverse transformation. A sufficient condition for this is that the Jacobian $J = \frac{\partial \eta}{\partial z}$ of the transformation must be strictly positive

$$J > 0, \quad (2.20)$$

since terrain-following coordinates based on the height z usually have the property, that η increases with increasing z .

Using (2.19), this yields

$$\frac{\partial z}{\partial \eta} = 1 - h_1 \frac{\cosh((H - \eta)/s_1)}{s_1 \sinh(H/s_1)} - h_2 \frac{\cosh((H - \eta)/s_2)}{s_2 \sinh(H/s_2)} > 0$$

Since the hyperbolic cosine terms have their maxima at $\eta = 0$, the condition reduces to:

$$\alpha_{inv} = \alpha_{1,inv} + \alpha_{2,inv} < 1 \quad (2.21a)$$

where the 'invertibility factor' α_{inv} . The two scale-dependent contributions are given by

$$\alpha_{1,inv} = \frac{\max_{x,y} h_1(x,y)}{s_1} \coth\left(\frac{H}{s_1}\right) \quad \alpha_{2,inv} = \frac{\max_{x,y} h_2(x,y)}{s_2} \coth\left(\frac{H}{s_2}\right) \quad (2.21b)$$

have been introduced. Since the maxima of the topography parts are uniquely defined by the splitting of the topography (see Section 4.2.1), Eq. (2.21) poses a restriction on the choice of s_1 and s_2 . In practice, the rate of decay of the large-scale part with height may depend on the application, where on the other hand, one will be interested in a rapid decay of the small-scale terrain features.

Since the maximum of $h_2(x, y)$ is generally smaller than the maximum of $h(x, y)$, the scale-height s_2 can be chosen smaller than the scale-independent scale-height s for the full topography without violating the invertibility condition. Therefore, small-scale terrain features in the level-heights can decay more rapidly than in the scale-independent case, which is a distinctive advantage of the new coordinate.

In Fig. 2.3 isolines of the invertibility factor α_{inv} as a function of the two scale heights s_1 and s_2

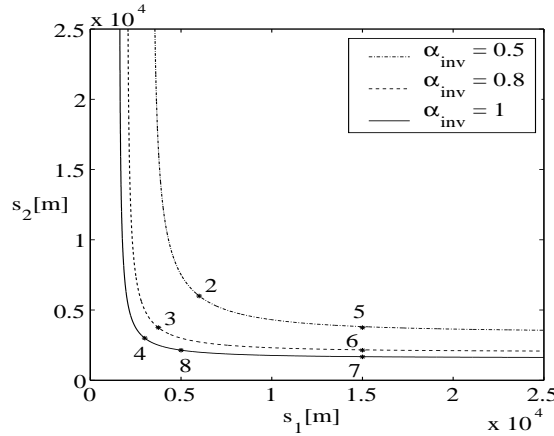


Figure 2.3: Isolines of the invertibility factor $\alpha_{inv}(s_1, s_2)$. For the description of the symbols see text.

are shown. The values of H and of the maxima of h_1 and h_2 are given by 25000 m, 1500 m and 1500 m respectively, which correspond to the values used in the numerical experiments described in Chapter 3. The thick contour bounds the region of the permissible scale heights. Additionally the contours $\alpha_{inv} = 0.5$ and 0.8 are plotted. Each star defines a pair of scale-heights and thus a representation for one specific coordinate transformation. The labels of the stars refer to the experiments described in Chapter 3, where the influence of the choice of s_i on the transformation error is investigated.

Chapter 3

An idealized 2D Advection Study

In this chapter, a numerical study is presented, which compares the performance of the new scale-dependent vertical coordinate introduced in *Chapter 2* with two other vertical coordinates in a simple numerical model. [Schär \(2000b\)](#) indicated that currently used terrain-following coordinates have serious problems to accurately represent horizontal advection over complex topography and that with the new scale-dependent coordinate the transformation error can be substantially reduced. The numerical study involves horizontal linear advection of a passive tracer $\phi(x, z, t)$ over complex topography.

3.1 Description of the Model

Setup

The advection study is performed in the domain described in *Eq. (2.2)*, which is bounded below by a complex topography containing a \cos^2 -shaped large-scale part and a superimposed small-scale part:

$$h(x) = h_1(x) + h_2(x) \quad (3.1a)$$

with

$$h_1(x) = \begin{cases} 0 \text{ m} & : |x| > a \\ \tilde{h}_1 \cos\left(\frac{\pi x}{2a}\right)^2 & : |x| \leq a \end{cases}, \quad h_2(x) = \frac{\tilde{h}_2}{\tilde{h}_1} \cdot h_1(x) \cdot \cos\left(\frac{2\pi x}{\lambda_2}\right) \quad (3.1b)$$

\tilde{h}_i refers to the height of the topography, a to the halfwidth of the large-scale ridge and λ_2 to the wavelength of the small-scale feature. The basic state wind profiles of U and \bar{w} are defined as

$$U(z) = \begin{cases} U_0 & : z_{s2} < z \leq H \\ U_0 \frac{z - z_{s1}}{z_{s2} - z_{s1}} & : z_{s1} < z \leq z_{s2} \\ 0 \text{ m/s} & : 0 \leq z \leq z_{s1} \end{cases}, \quad \bar{w} = 0 \text{ m/s} \quad (3.2)$$

H refers to the upper lid of the model. This corresponds to a stagnant layer directly above the topography separated by a shear layer from uniform horizontal wind U_0 aloft. A \cos^2 -shaped tracer anomaly of amplitude 1 and radius 3000 *m* is placed at a height of 6800 *m*, sufficiently high, that it does not interact with the terrain and does not overlap with the shear layer. In *Table 3.1* the values of all variables of the setup are specified.

x_{min}	$-75000\ m$	H	$25000\ m$	\tilde{h}_1	$1500\ m$	a	$25000\ m$	z_{s_1}	$3200\ m$
x_{max}	$75000\ m$	U_0	$10\ m/s$	\tilde{h}_2	$1500\ m$	λ_2	$8000\ m$	z_{s_2}	$3800\ m$

Table 3.1: Variables and corresponding values of the setup of the idealized 2d advection study (c.f. Eq. (3.1) and Eq. (3.2))

Prognostic Equation and Coordinate Transformation

The mass conservation equation of the passive tracer $\phi(x, z, t)$ in two spacial dimensions reads

$$\frac{\partial \phi}{\partial t} + \frac{\partial(U\phi)}{\partial x} + \frac{\partial(\bar{w}\phi)}{\partial z} = 0 \quad (3.3)$$

where U and \bar{w} are specified by Eq. (3.2) and Table 3.1. Thus, the only dynamic field is that of the passive tracer $\phi(x, z, t)$. In order to solve this equation in the computational space, it has to be transformed to η -coordinates as described in Section 2.3. With the aid of Eq. (2.17) the transformed equivalent to Eq. (3.3) can be derived:

$$\frac{\partial(J^{-1}\phi)}{\partial t} + \frac{\partial(UJ^{-1}\phi)}{\partial x} + \frac{\partial(\dot{\eta}J^{-1}\phi)}{\partial z} = 0. \quad (3.4)$$

Here, $\dot{\eta} = \frac{D\eta}{Dt}$ is the vertical velocity expressed in the reference of the new vertical coordinate and $J = \frac{\partial \eta}{\partial z}$ is the Jacobian of the transformation.

Discretization

The flux-form of Eq. (3.4) is discretized in the computational η -space on a horizontally and vertically staggered grid with centered differences in space and without explicit horizontal diffusion. Time discretization is performed with centered differences and the application of the Asselin time-filter (Asselin, 1972) to suppress the short-frequency solutions generated by the leapfrog scheme. Schär (2000b) tested other, more sophisticated schemes for the advection study, but obtained qualitatively similar results. The Jacobian is computed analytically, evaluated on the grid points and stored in a two-dimensional array. A horizontal resolution of $\Delta x = 1000\ m$ ensures that even the small-scale terrain features have a wavelength of $8\Delta x$ and are thus well resolved. In the vertical, a uniform spacing of the 50 computational levels ($\Delta \eta = 500\ m$) is chosen. The timestep of the integration has a value of $\Delta t = 25\ s$ which results in a horizontal Courant number ($U_0 \frac{\Delta t}{\Delta x}$) = 0.25. The vertical Courant number in η -coordinates ($\dot{\eta} \frac{\Delta t}{\Delta \eta}$) depends on the coordinate transformation, but never exceeds 0.5.

3.2 Experiments

In order to compare the different vertical coordinates, several numerical runs are performed:

- Run 0:** A case without topography, and thus with simple z -coordinates, serves as a reference for all other runs and allows for the determination of the truncation error caused solely by the numerical scheme (Fig. 3.1a).
- Run 1:** Applies the Gal-Chen coordinate Eq. (2.8), which is widely used in today's non-hydrostatic NWP models (Fig. 3.1b).
- Run 2:** Employs an exponential coordinate. Its vertical decay function is given by Eq. (2.13). A scale height of $s = 6000 \text{ m}$ yields a much faster decay with height of the terrain features as compared to the Gal-Chen coordinate.
- Run 3:** As Run 2, but with a scale height of $s = 3750 \text{ m}$ (Fig. 3.1c).
- Run 4:** As Run 2, but with a scale height of $s = 3000 \text{ m}$.
- Run 5:** Uses the new, scale-dependent coordinate Eq. (2.15) with scale heights of $s_1 = 15000 \text{ m}$ and $s_2 = 3750 \text{ m}$.
- Run 6:** As Run 5, but with scale heights of $s_1 = 15000 \text{ m}$ and $s_2 = 2140 \text{ m}$ (Fig. 3.1d).
- Run 7:** As Run 5, but with scale heights of $s_1 = 15000 \text{ m}$ and $s_2 = 1666 \text{ m}$.
- Run 8:** As Run 5, but with scale heights of $s_1 = 5000 \text{ m}$ and $s_2 = 2140 \text{ m}$.

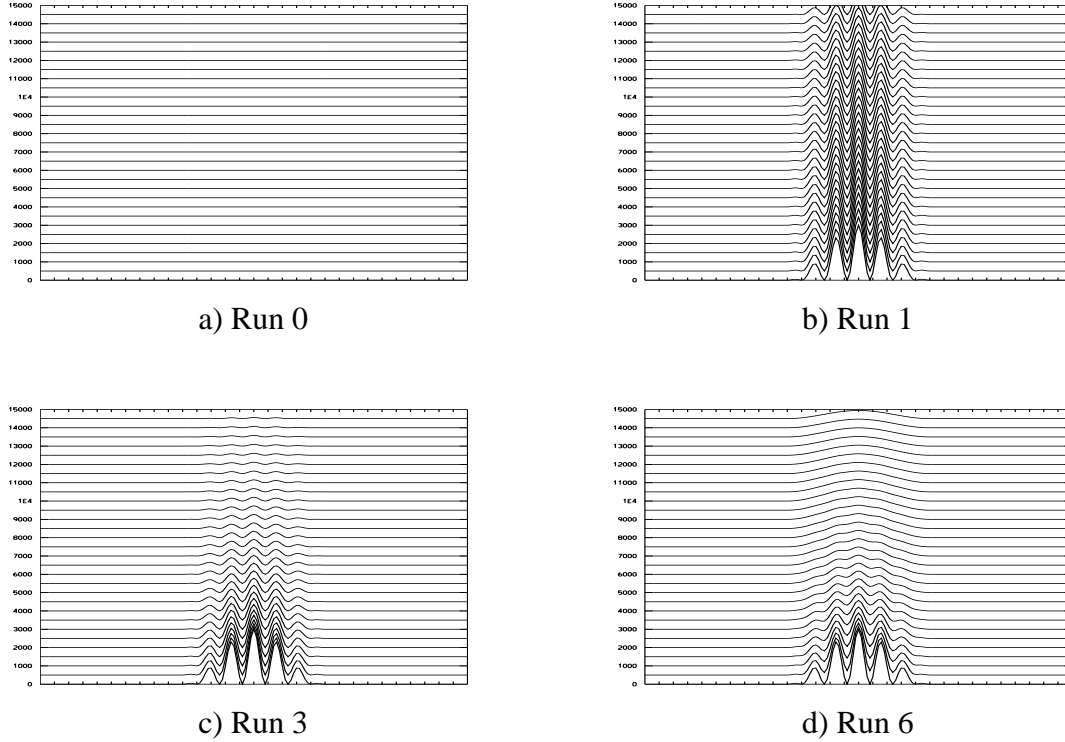


Figure 3.1: Topography and height of the computational levels of selected numerical Runs. a) Reference case without topography, b) Gal-Chen coordinate (Run 1), c) Exponential coordinate (Run 3), d) New, scale dependent coordinate (Run 6). The diagrams show only the lower 15000 m of the domain. The horizontal spacing of the ticks is $5\Delta x$.

3.3 Results

The results obtained with the 2D advection study confirm those presented by [Schär \(2000b\)](#). [Fig. 3.2](#) shows the results of selected Runs. In the left panels, the computed tracer field of ϕ is plotted at start-time, mid-time and end-time of the integration. The right panels show the absolute error (difference of computed ϕ and analytical solution) at end-time. The absolute maximum values of the respective errors are indicated in the plots. In [Table 3.2](#) an overview of all Runs and the respective maximal absolute error is shown.

The relative truncation error of the numerical scheme is approximately 2% of the anomaly's maximal amplitude (Run 0). A considerable coordinate transformation error is caused by the Gal-Chen coordinate (Run 1). It is larger by one order of magnitude as compared to the truncation error. This is not very surprising if we take a look at the shape of the computational levels ([Fig. 3.1b](#)). At the height of the anomaly, the terrain features in the computational levels are only slightly damped, causing a highly distorted transformation of horizontal flow features.

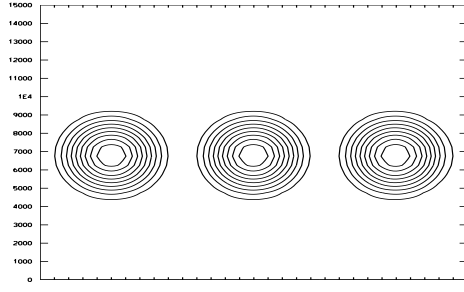
Much better results are obtained with the exponential coordinate, a successive decrease of the scale height results in a reduction of the transformation error (Runs 2-4). The choice of an invertibility factor $\alpha_{inv} = 1$ makes clear, that at least in this simple numerical model, the invertibility condition need not be very stringently satisfied. The result of Run 4 shows that the transformation error almost vanishes, when the smallest possible scale-height is chosen, and the difference to the results obtained with the reference case are only minor.

The Runs with the new, scale-dependent coordinate yield similar results. A sensitivity study

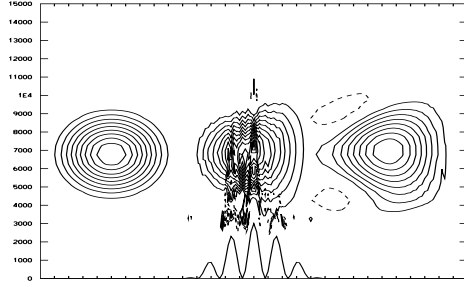
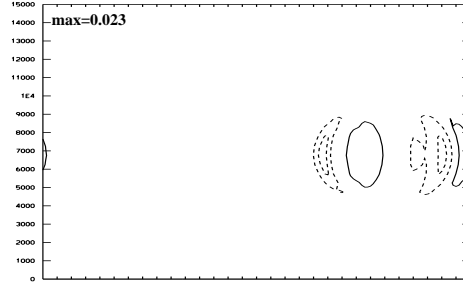
for the scale-heights s_i shows, that the transformation error is more strongly influenced by the small-scale terrain-induced noise in the heights of the computational levels, than by the large-scale noise. A decrease in s_2 by a factor of 1.75 (Runs 5 and 6) yields a decrease of the error by a factor of 2.4. On the other hand, a decrease in s_1 by a factor of 3 (Runs 6 and 8) has practically no influence on the error. If we compare the scale-dependent coordinate with the scale-independent coordinate we note, that the difference in the performance decreases with an increasing invertibility factor α_{inv} (Runs 2 and 5, 3 and 6, 4 and 8). The explanation for this effect is, that at the height of the anomaly the difference between the coordinates with a large invertibility factor are negligible, which is not the case for smaller factors. Thus, for the most rapid vertical decay of the terrain features and for this simple advection test, the benefit of the scale dependent decay is comparatively minor. Nevertheless, the best results are obtained with the scale-dependent coordinate, where both parts of the topography decay very fast with height (Run 8).

Exp.	Coordinate	s_1	s_2	$\alpha_{1,inv}$	$\alpha_{2,inv}$	α_{inv}	Error
0	z	-	-	-	-	-	0.023
1	Gal-Chen	-	-	-	-	-	0.350
2	Exponential	6000 m	-	0.5	-	0.5	0.120
3	Exponential	3750 m	-	0.8	-	0.8	0.037
4	Exponential	3000 m	-	1.0	-	1.0	0.027
5	New	15000 m	3750 m	0.1	0.4	0.5	0.061
6	New	15000 m	2140 m	0.1	0.7	0.8	0.025
7	New	15000 m	1666 m	0.1	0.9	1.0	0.024
8	New	5000 m	2140 m	0.3	0.7	1.0	0.023

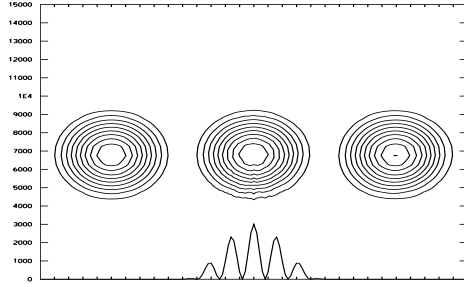
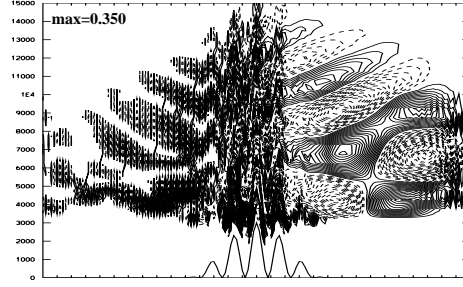
Table 3.2: Results of Runs 0 - 8 of the 2D-advection study. For the description of the variables see text.



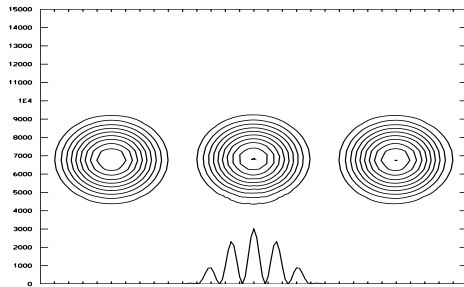
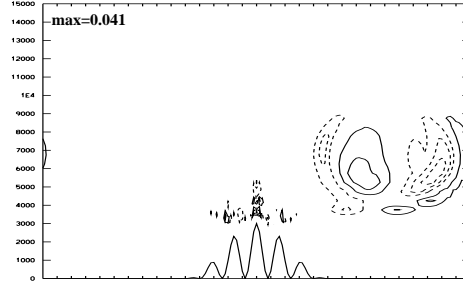
a) Run 0



b) Run 1



c) Run 3



d) Run 6

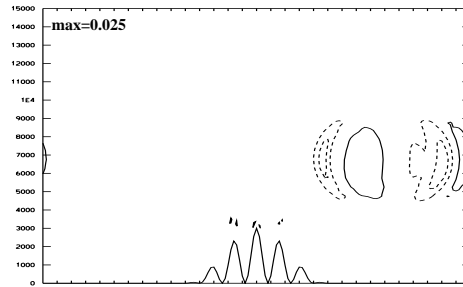


Figure 3.2: Selected results of the 2D-Advection test. Left panel shows computed solution at start-time, mid-time and end-time (contour interval is 0.1). Right panel shows absolute error (difference between computed and exact solution) at end-time. (dashed: negative values, solid: positive values, contour interval is 0.01, maximal absolute error as indicated). a) Reference case without topography, b) Gal-Chen coordinate, c) Exponential coordinate, d) New, scale dependent coordinate. The diagrams show only the lower 15000 m of the domain. The horizontal spacing of the ticks is $5\Delta x$.

Chapter 4

Application in a High-Resolution Atmospheric Model

In this chapter, the new coordinate is implemented and tested in a non-hydrostatic regional forecast model. In the first section, the Mesoscale Compressible Community (MC2) model is briefly introduced. In the second section, some technical issues of the implementation of the new coordinate are discussed, while in the third section, idealized numerical case studies are presented.

4.1 The MC2 Model

Early numerical forecast models were concerned with synoptic-scale dynamics, where the horizontal scale of interest is about two orders of magnitude larger than the vertical scale, i.e. the atmospheric flow is nearly in hydrostatic balance and vertical accelerations are negligible. Applying the hydrostatic assumption allows for a much larger time step for the stable integration of the governing equations with explicit schemes. With the ongoing revolution of computing resources, the development of more efficient numerical methods and the improvements of meteorological measurements, the trend in atmospheric research leads towards the simulation of mesoscale phenomena and towards more accurate regional forecasts. On this scale the hydrostatic assumption is no longer justified and non-hydrostatic models have to be used. Moreover, especially in mountainous regions, the inclusion of topography and the choice of an appropriate vertical coordinate is inevitable.

The MC2 model developed at *Recherche en prévision numérique (RPN)*, *Environment Canada* and the *University of Montreal* ([Tanguay et al. \(1990\)](#), [Benoit et al. \(1997\)](#), [Thomas et al. \(1998\)](#), [Bergeron et al. \(1994\)](#)) was designed to simulate atmospheric phenomena on a wide range of scales, reaching from large-scale synoptic flow down to mesoscale flow over steep mountains. It is used by several research groups around the world and has been successfully run with an unprecedented resolution of 3 km and in an operational mode during the field phase (1999) of the *Mesoscale Alpine Programme (MAP)*, see [Benoit et al. \(2002\)](#). In the remainder of this section a short overview of the physical and numerical aspects of the MC2 is given.

Governing Equations

MC2 applies the fully compressible Euler equations, describing the dynamics of a compressible gas. They consist of the conservation of momentum, mass, energy and specific humidity. Together with the equation of state for an ideal gas a set of six prognostic equations for the six dynamical variables u, v, w, p, T, M and one diagnostic equation for ρ is formed, where the variables denote

the three velocity components, pressure, temperature, water vapour content and density, respectively. It is worth noting that this unfiltered set of equations supports waves on an extremely wide range of scales from Rossby waves on a planetary scale to sound waves on the micro scale. With the use of sophisticated numerical schemes it is possible, to efficiently integrate these equations at a time resolution which is prescribed by the physical phenomenon of interest.

In addition to the dynamic treatment of atmospheric flow, a physics package can be linked to the MC2 model, which considers subgrid scale physical processes and includes according parametrizations like turbulence, condensation and precipitation, the treatment of the turbulent boundary layer or the exchange of heat and moisture with the soil. In this study, however, the physical package is not used.

Discretization

Since the compressible Euler equations support the fast moving sound waves it is crucial for the efficient integration of larger scale phenomena that the numerical scheme allows for a sufficiently large time step. MC2 uses a semi-implicit semi-Lagrangian scheme. The implicit treatment of all pressure gradient terms can permit a time step which is one to two orders of magnitude larger than a time step required for a stable integration with an explicit scheme. For slowly varying flows the semi-Lagrangian formulation can improve efficiency additionally. The semi-implicit formulation requires the solution of an elliptic Helmholtz equation for pressure at each time step. A Generalized Minimal Residual (GMRES) Krylov type solver is applied for this purpose. The spatial discretization is performed with horizontal second order centered differences on the staggered Arakawa-'C' grid ([Arakawa, 1977](#)) and vertical second order centered differences on a vertically staggered grid.

Vertical coordinate

The original version of MC2 uses the hybrid vertical coordinate given by *Eq. (2.9), (2.11) and (2.12)*. A generalized vertical coordinate is obtained by applying a second transformation $Z(\eta)$, thus allowing for an arbitrary spacing of the computational levels (c.f. *Figure 2.1*).

4.2 Implementation of the New Coordinate into MC2

In this section two aspects of the implementation of the new coordinate into the MC2 code are described. The code version used for the implementation is MC2 v4.9.1. Daniel Lüthi from ETH Zürich and Claude Girard from RPN, Canada have provided the ability to store fully 3D metric terms, which allows for the application of a wide variety of scale-independent vertical coordinates. This study includes the extension of the code for the use of a scale-dependent vertical coordinate. In a first subsection the splitting of the topography into a large-scale and a small-scale part is presented, while the second subsection deals with the calculation of the metric terms of the new coordinate formulation.

4.2.1 Splitting of the Topography

The key feature of the new coordinate formulation is the separate vertical decay of the large-scale and the small-scale terrain features. For the calculation of the computational level-heights *Eq. (2.15)* and *(2.16)* can be used. The large-scale part h_1 of the topography can be obtained by the application of a smoothing digital filter to the full topography h . The small-scale part h_2 is computed with *Eq. (2.14)*. In this study a simple first order digital filter is used. The relation between h_1 and h is given by

$$[h_1] = F^\nu [h] \quad (4.1)$$

where $[h_1]$ and $[h]$ refer to the discretized topographies. The filter operator F is given by the stencil

$$F = \begin{bmatrix} 0 & 0 & 0 \\ 1/4 & 1/2 & 1/4 \\ 0 & 0 & 0 \end{bmatrix} \quad (4.2)$$

in the case where h is a function of x only and by the stencil

$$F = \begin{bmatrix} 0 & 1/8 & 0 \\ 1/8 & 1/2 & 1/8 \\ 0 & 1/8 & 0 \end{bmatrix} \quad (4.3)$$

in the general case. The parameter ν determines the number of applications and is chosen as $\nu = 100$ for this study. Boundary points are left unchanged in the filtered topography. The filter removes all small-scale variations in h of wavelengths shorter than $15\Delta x$ by a factor of at least 98.7%. The cutoff is relatively smooth, so modes of larger wavelengths are also damped. In *Figure 4.1* the response function of the filter is shown.

In *Figure 4.2* h and h_1 for the topography given by *Eq. (3.1)* are shown. Note that the $8\Delta x$ -waves are almost completely damped in h_1 . A filter of this type is well suited for the topography used in this study. However, for more complex topography the choice of a more sophisticated filter has to be considered for mainly three reasons: Firstly, the treatment of the boundary points becomes non-trivial when the topography is not smooth along the boundaries. Secondly, the response function of the filter given by *Eq. (4.3)* is not rotationally symmetric, thus the effect of the filter is dependent on the direction of the variations. Thirdly, in order to choose a small scale-height s_2 for the new coordinate, it is desirable for the amplitude of h_2 be as small as possible (c.f. *Eq. (2.21)*). Thus, a strong damping of large-scale features is not desired. More sophisticated filters can be obtained by increasing the order, which improves the scale-selection of the filter and decreases the number of applications necessary to remove small-scale features. For the construction of higher order filters suited for limited-area fields we refer to ([Raymond, 1988](#)).

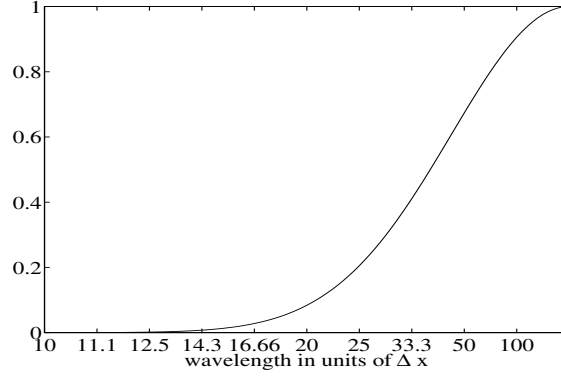


Figure 4.1: Response function for the filter used to split the topography in a small-scale and a large-scale part. For the definition of the filter see text.

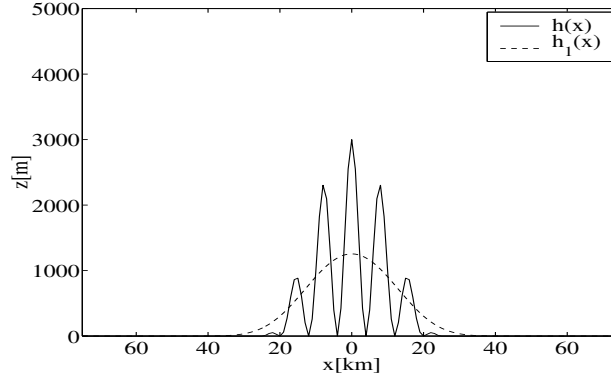


Figure 4.2: Splitting of the topography h (solid) given by Eq. (3.1) in a large-scale part h_1 (dashed) and a small-scale part h_2 (not shown)

4.2.2 Treatment of the Metric Terms

In this section the treatment of the metric terms in the code is shortly described. In MC2 the vertical coordinate transformation is treated as described in Section 2.1. The computational space is spanned by generalized Z coordinates, which allows for a non-uniform spacing of the computational levels. In earlier formulations, the vertical coordinate transformation was hard-coded, which restricted the model to the use of just one particular transformation. With the formulation of the new coordinate it is more efficient to store the relevant metric terms of the transformation in three-dimensional arrays, which makes the choice of the vertical coordinate more flexible. The impact of these changes on memory requirements and runtime is comparatively minor.

The Grid used in MC2

Before defining the discretization of the metric terms it is worth shortly describing the type of grid used in MC2. There are two vertically staggered grids, one with full k indices and one with $k - 1/2$ indices, shifted by one half ΔZ . The vertical arrangement of the model levels and variables is depicted in Figure 4.3. The variables U , V , W , w and w_s denote the three velocity components in the computational coordinate system, the vertical velocity and its diagnostic value at the surface in the cartesian coordinate system, respectively. The other variables shown in the figure will be introduced later in this section. The horizontal discretization is performed on the

Arakawa-'C' grid. On this staggered grid, the velocities are shifted one half grid-length in x and y -direction respectively. The horizontal arrangement of the grid points and the variables is depicted in [Figure 4.4](#).

Computation and Discretization of Metric Terms

The relevant metric terms of the transformation are computed from the transformation

$$z_{lev}(x, y, \eta) = \eta + h_1(x, y)b_1(\eta) + h_2(x, y)b_2(\eta) \quad (4.4)$$

where z_{lev} denotes the physical height of the computational level η and the b_i are defined by [Equation \(2.15\)](#). A second transformation $Z(\eta)$ is applied (see [Section 2.1](#)), thus the metric terms can be written as

$$\begin{aligned} G_0 &= \frac{\partial z_{lev}}{\partial Z}, & G_1 &= -\left(\frac{\partial z_{lev}}{\partial x}\right)_Z, & G^{13} &= \left(\frac{\partial Z}{\partial x}\right)_{z_{lev}} = \frac{G_1}{G_0}, & F_1 &= -\frac{1}{G_0} \frac{\partial G_0}{\partial x} \\ G_2 &= -\left(\frac{\partial z_{lev}}{\partial y}\right)_Z, & G^{23} &= \left(\frac{\partial Z}{\partial y}\right)_{z_{lev}} = \frac{G_2}{G_0}, & F_2 &= -\frac{1}{G_0} \frac{\partial G_0}{\partial y} \end{aligned}$$

where the notation corresponds to the one used in [\(Bergeron et al., 1994\)](#).

For the development of the relations above [Eq. \(2.17\)](#) is used. The discretization of the metric terms can be done by taking finite differences of z_{lev} on the computational grid:

$$\begin{aligned} [G_0]_{i,j,k} &= [\delta_Z z_{lev}]_{i,j,k} \\ [\overline{G_1^Z}]_{i-1/2,j,k} &= -[\overline{\delta_x z_{lev}^Z}]_{i-1/2,j,k} & [\overline{G_2^Z}]_{i,j-1/2,k} &= -[\overline{\delta_y z_{lev}^Z}]_{i,j-1/2,k} \\ [G_1]_{i,j,k} &= [\overline{\overline{G_1^Z}^x}]_{i,j,k} & [G_2]_{i,j,k} &= [\overline{\overline{G_2^Z}^y}]_{i,j,k} \\ [G^{13}]_{i-1/2,j,k} &= \left[\frac{\overline{G_1^Z}}{\overline{G_0^x}}\right]_{i-1/2,j,k} & [G^{23}]_{i,j-1/2,k} &= \left[\frac{\overline{G_2^Z}}{\overline{G_0^y}}\right]_{i,j-1/2,k} \\ [F_1]_{i,j,k} &= -\left[\frac{\overline{\delta_x G_0^x}}{G_0}\right]_{i,j,k} & [F_2]_{i,j,k} &= -\left[\frac{\overline{\delta_y G_0^y}}{G_0}\right]_{i,j,k} \end{aligned}$$

The finite difference operators are defined by

$$[\delta_r A]_l = \frac{A_{l+1/2} - A_{l-1/2}}{\Delta r}, \quad [\delta_r A]_{l-1/2} = \frac{A_l - A_{l-1}}{\Delta r}$$

where r stands for one of $\{x, y, Z\}$ and l stands for one of $\{i, j, k\}$, respectively. We have also introduced the interpolation operators to interpolate a variable to a grid point or a level, where it is not naturally defined:

$$[\overline{A^r}]_l = \frac{A_{l+1/2} + A_{l-1/2}}{2}, \quad [\overline{A^r}]_{l-1/2} = \frac{A_l + A_{l-1}}{2}$$

Alternative way of treating the Metric Terms

Another possibility to compute the metric terms, which has not been tracked in this study, but might be superior to the one described above, is the following. The metric terms can be rewritten as

$$G_0 = \frac{\partial z_{lev}}{\partial Z} = \frac{\partial z_{lev}}{\partial \eta} \frac{\partial \eta}{\partial Z}$$

$$G^{13} = \left(\frac{\partial Z}{\partial x} \right)_{z_{lev}} = \frac{\partial Z}{\partial \eta} \left(\frac{\partial \eta}{\partial x} \right)_{z_{lev}} \quad G^{23} = \left(\frac{\partial Z}{\partial y} \right)_{z_{lev}} = \frac{\partial Z}{\partial \eta} \left(\frac{\partial \eta}{\partial y} \right)_{z_{lev}}$$

$$F_1 = -\frac{1}{G_0} \frac{\partial G_0}{\partial x} = -\frac{1}{G_0} \left(\frac{\partial^2 z_{lev}}{\partial x \partial \eta} \right) \frac{\partial \eta}{\partial Z} \quad F_2 = -\frac{1}{G_0} \frac{\partial G_0}{\partial y} = -\frac{1}{G_0} \left(\frac{\partial^2 z_{lev}}{\partial y \partial \eta} \right) \frac{\partial \eta}{\partial Z}$$

where again Eq. (2.17) has been used. It is now possible to partially evaluate the terms involving η analytically, i.e to substitute these terms by Eq. (2.19). The only derivatives, which cannot be computed analytically and thus still must be approximated by finite differences are the partial derivatives of the topography parts, i.e.

$$\frac{\partial h_i}{\partial s}, \quad i = 1, 2 \quad s = \{x, y\}.$$

It is expected, that this approach will improve the order of accuracy of the computation of the level-heights and the metric terms, but the impact on the overall accuracy of the model cannot be clearly predicted. The investigation of this issue could be part of future work.

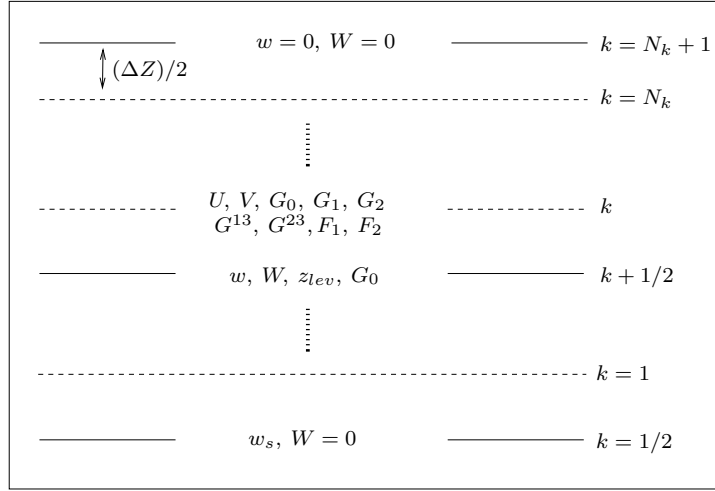


Figure 4.3: Vertical arrangement of the model levels and location of the variables on the grid. The index k is used to index the position according to the Z -axis. N_k is the number of computational levels.

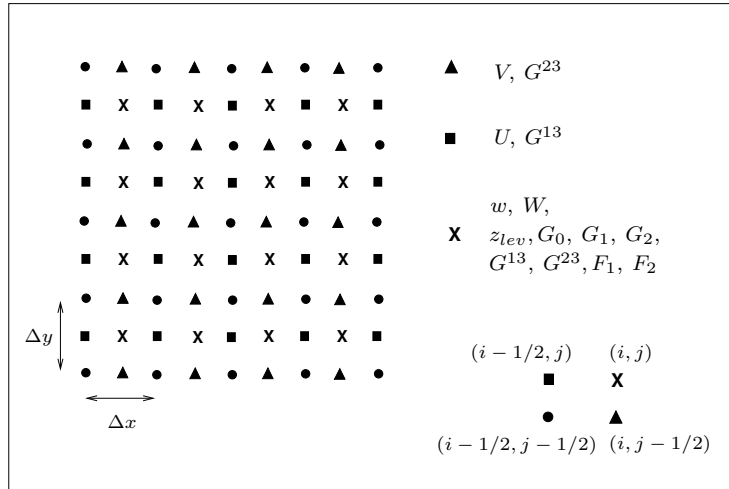


Figure 4.4: Schematic representation of the staggered grid and distribution of the variables used for horizontal discretization. The indices i and j are used to index the position according to the x -axis and y -axis respectively.

4.3 Idealized Case Studies

In this section two selected idealized case studies with the MC2 model are presented, which are intended to compare the accuracy of the new coordinate with that of the exponential coordinate and the *Gal-Chen* coordinate. All case studies were performed in the computing environment of the Swiss Center for Scientific Computing (CSCS) in Manno. The platform used for the computations was a NEC-SX5 parallel vector machine with 8 CPU, 64GB main memory and a theoretical peak performance of 8 GFLOPS per CPU.

Setup of the MC2 Model

The MC2 model was introduced in *Section 4.1*. Here we briefly define the general setup of the model, which is used for all case studies described in the remainder of this chapter. The settings, which are specific to the case studies are defined in the according subsections of the case studies. Since the MC2 is a limited area model, boundary values for all prognostic variables have to be described. In this study a basic state of the atmosphere is defined, which is used as initial condition and for a time-independent Davies-type nesting (*Davies, 1976*) at the lateral and the upper boundaries. The upper sponge, where the nesting is applied, consists of 30 levels, thus about half of the total vertical extent of the computational domain, the lateral nesting is applied within a boundary of 10 gridpoints. The model is impulsively started, since it is assumed, that the steady state solutions in this study do not seriously depend on the initialization procedure. All runs are performed without any explicit horizontal diffusion.

The atmosphere of the basic state used in this study has a uniform stratification, i.e. $N = \sqrt{\frac{g}{\theta} \frac{\partial \theta}{\partial z}} = 0.01 \text{ s}^{-1}$, where N is the Brunt-Väisälä frequency, θ the potential temperature and g the gravitational acceleration. Together with the sea level ($z = 0 \text{ m}$) temperature $T_0 = 288 \text{ K}$ and pressure $p_0 = 10^5 \text{ Pa}$ the basic state profiles of the temperature and the pressure can be determined. The basic state wind velocities are $V = \bar{w} = 0 \text{ m/s}$ and the wind profile of U depends on the case studies.

4.3.1 Case study 1: Stagnant Layer over 3D-Topography

The case study described in this subsection is the logical extension of the 2D advection study described in *Chapter 3* to full dynamics and three dimensions. A smooth 3D Gaussian hill fully embedded in a stagnant layer is capped by a shear layer and uniform wind aloft. The analytical solution of this problem for all times is simply the state at $t = 0 \text{ s}$. The difference between the three coordinates in the computation of the steady state flow is investigated for different heights and halfwidths of the hills.

Setup

The domain under consideration is described by Eq. (2.2) and is bounded below by a smooth Gaussian hill

$$h(x) = \tilde{h} \exp \left[- \left((x/a)^2 + (y/a)^2 \right) \right], \quad (4.5)$$

where \tilde{h} and a denote the mountain height and the halfwidth, respectively. The wind profiles of U and \bar{w} are defined by Eq. (3.2). The height of the stagnant layer is located more than 1000 m above the topography. Thus the mountain lies completely within this stagnant layer. In Table 4.1 the values of selected variables of the setup are specified.

x_{min}	-118000 m	y_{min}	-150000 m	H	19500 m	z_{s_1}	2000 m
x_{max}	182000 m	y_{max}	150000 m	U_0	10 m/s	z_{s_2}	4000 m

Table 4.1: Variables and corresponding values of the setup of case study 1. For a description of the variables see Eq. (3.1) and Eq. (3.2)

The horizontal spacial resolution of the model is defined by $\Delta x = \Delta y = 2000 \text{ m}$ resulting in $N_i = N_j = 150$ gridpoints. The vertical spacing of the 65 computational levels is uniform and

$$\Delta z = \Delta \eta = \Delta Z = 300 \text{ m}.$$

The integration time is chosen sufficiently large, ensuring that the flow is in a steady state. Experience has shown, that a dimensionless integration time of $\hat{t} = t \cdot U_0/L = 6$, where L is the horizontal extent of the domain, satisfies well this requirement (c.f. Fig. 4.6d-f) and Fig. 4.7d-f). The timestep was chosen as $\Delta t = 30 \text{ s}$ resulting in 6000 timesteps. This choice results in advective Courant numbers of approximately 0.15 (horizontally) and 0.04 (vertically).

Experiment 1

A first experiment compares the flow computed with the three coordinates with scale-heights of $s = 3000 \text{ m}$, $s_1 = 4000 \text{ m}$ and $s_2 = 2000 \text{ m}$. These values are chosen according to a realistic topography like the alps with amplitudes up to 4000 m . Different heights and halfwidths of the mountains are chosen:

Run 0: A run without topography, and thus equivalent to z -coordinates.

Run 1: A Gaussian hill with a height of $\tilde{h} = 250 \text{ m}$ and a halfwidth of $a = 10000 \text{ m}$.

Run 2: As Run 1 but with $\tilde{h} = 500 \text{ m}$ and $a = 10000 \text{ m}$.

Run 3: As Run 1 but with $\tilde{h} = 250 \text{ m}$ and $a = 20000 \text{ m}$.

Run 4: As Run 1 but with $\tilde{h} = 500 \text{ m}$ and $a = 20000 \text{ m}$.

Runs 1-4 were performed with all three coordinates. The topography is split as described in Section 4.2.1 with the filter defined by Eq. (4.3). The invertibility factor for the different hills never exceeds values of $\alpha_{inv} = 0.2$. In Figure 4.5 the steady state solution without topography is shown. The left Panel a shows a vertical cross-section of the vertical velocity w at $y = 0 \text{ m}$. Beside of the boundary effects, the correct physical wind of $w = 0 \text{ m/s}$ is well approximated. The right Panel b shows a vertical cross section of the horizontal velocity u at $y = 0 \text{ m}$. The contour interval is 0.5 m/s and the shear layer between 2000 m and 4000 m is visible. These

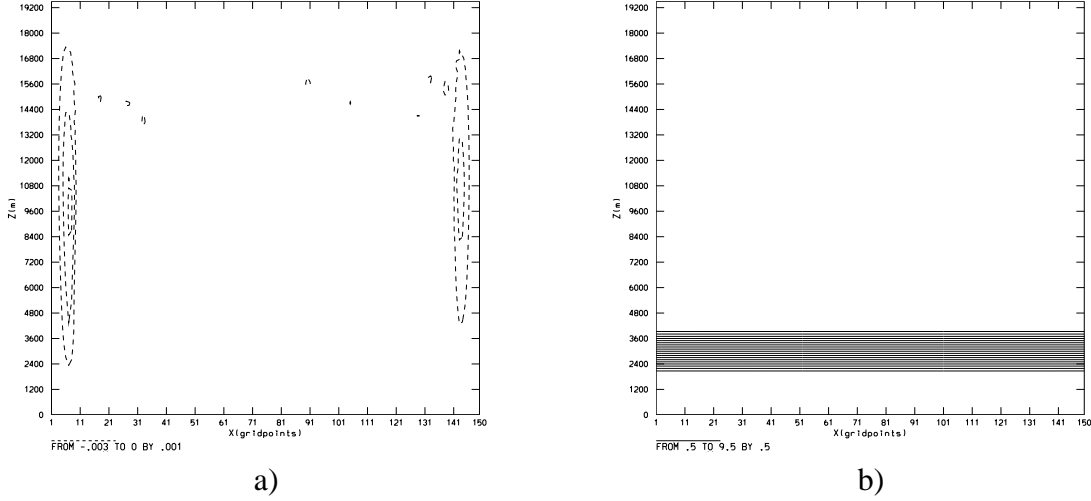


Figure 4.5: Results of Experiment 1, Run 0. Vertical cross-sections of the vertical velocity w (Panel a, contour interval is 0.001 m/s) and horizontal velocity u Panel b, contour interval is 0.5 m/s) at $y = 0 \text{ m}$. Positive contours are solid, negative are dashed.

results show that without topography and thus equivalent to z -coordinates, the analytical solution of the problem is well reproduced.

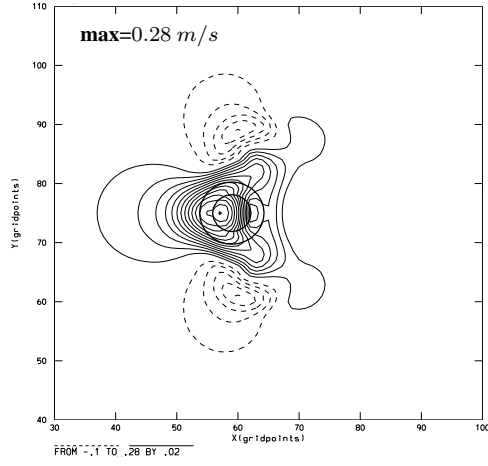
If the topography is included and terrain-following coordinates are applied, an error appears in the computed flows. Since the analytical solution of u is identically zero for $z \leq z_{s1} = 2000 \text{ m}$ and those of v and w are zero throughout the whole domain, and since the computation with z -coordinates yields a very good approximation of this analytical solution, the errors appearing in the solutions computed with the terrain-following coordinates must be solely caused by the coordinate transformation. This fact allows for a quantitative comparison of the vertical coordinates. Since in this experiment no small-scale features occur in the topography, the difference between the exponential and the new coordinate is expected to be minor. Several comparison runs, which are not shown here, confirmed this assumption and therefore the results of the runs of Case study 1 with the exponential coordinate are not shown. In Fig. 4.6 cross-sections of the computed u -component of the velocity for a Gaussian hill of $\tilde{h} = 250 \text{ m}$ and $a = 10000 \text{ m}$ computed with the *Gal-Chen* coordinate are shown. Figure 4.7 shows the same cross-sections computed with the new coordinate. Figure 4.7a and Fig. 4.7b show horizontal cross-sections of u and v at $z = 1800 \text{ m}$ which is located directly below the upper boundary of the stagnant layer. Figure 4.7d and Fig. 4.7e show the maxima (dash-dotted) and minima (dashed) of the horizontal flow fields computed using

$$\begin{aligned}
 A_{max}^t &= \max_{i,j,k} A(i, j, k, t) - \max_{i,j,k} A(i, j, k, t = 0) \quad \text{and} \\
 A_{min}^t &= \min_{i,j,k} A(i, j, k, t) - \min_{i,j,k} A(i, j, k, t = 0),
 \end{aligned}
 \tag{4.6}$$

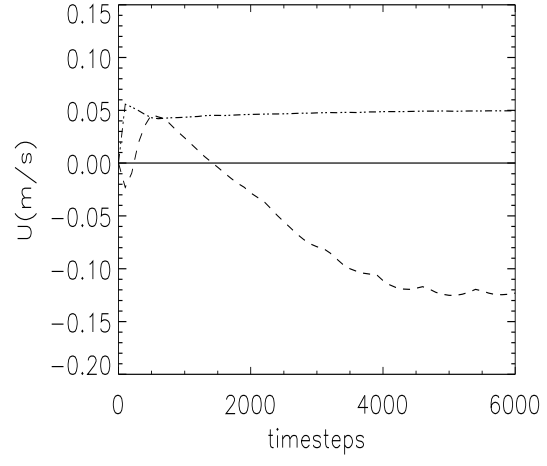
where the indices i, j, k run across the whole domain and A stands for one of $\{u, v, w\}$. From these plots one can see, that the flow reaches a steady state after approximately 6000 timesteps. It is also evident, that the new coordinate reduces the transformation error as compared to the *Gal-Chen* coordinate. For the new coordinate, the error seems to originate in the shear layer and propagate upwards as a mountain wave. For the *Gal-Chen* there seem to be sources of error even above the shear layer. This can be explained by the exponential (resp. linear) decay of terrain features for the new (resp. *Gal-Chen*) coordinate. The reduction of the error is apparent in all fields, but the vertical velocity w is most sensitive to it as can be seen from the maxima and minima of the

fields. Thus, hereafter, we will concentrate on the vertical velocity alone for the comparison of the coordinates and will not further discuss the horizontal velocity components.

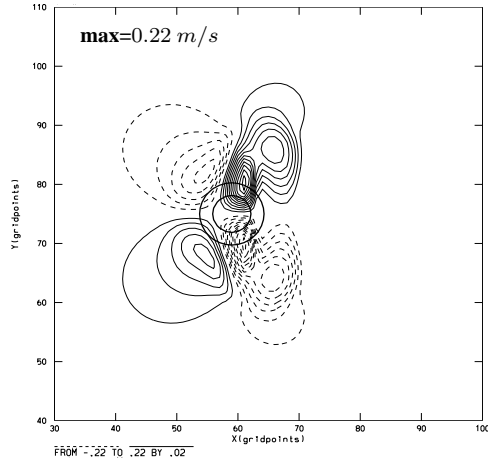
As a next step, the effect of the height and the halfwidth of the Gaussian hill on the transformation error is examined. *Figure 4.8* shows the computed vertical velocities for different hill dimensions. The left and right panels show cross-sections computed with the *Gal-Chen* and new coordinate respectively. For all four hill dimensions the error is reduced by up to a factor of 4, if the new coordinate is applied. The results indicate, that the deviation from the analytical solution scales approximatively with the height \tilde{h} , i.e. the amplitude is doubled if the height is doubled. Such a simple scaling law is not apparent for the halfwidth a . However, the amplitude of the error is larger for a narrow mountain. The effect of the transformation error clearly increases with decreasing resolution of the terrain features. This indicates that the benefit of the new coordinate increases with decreasing horizontal scale of the topography features. Again the error caused by the new coordinate seems to be originated at the height of the shear layer forcing wave-type features, while source of the error caused by the *Gal-Chen* coordinate is likely to be located also in higher regions.



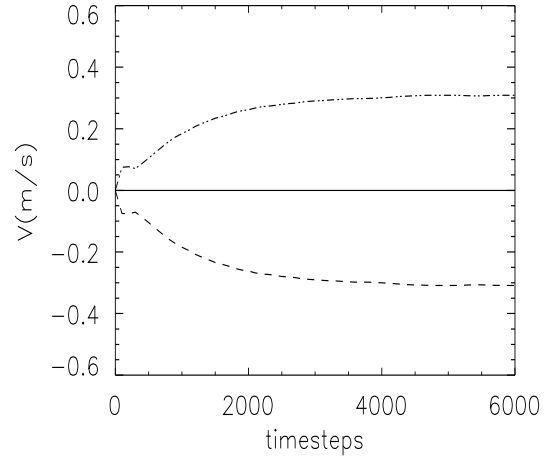
a)



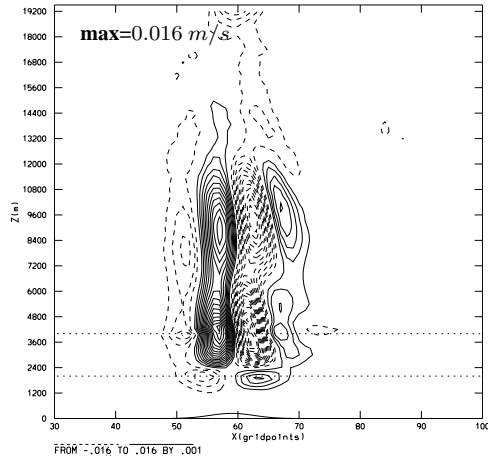
d)



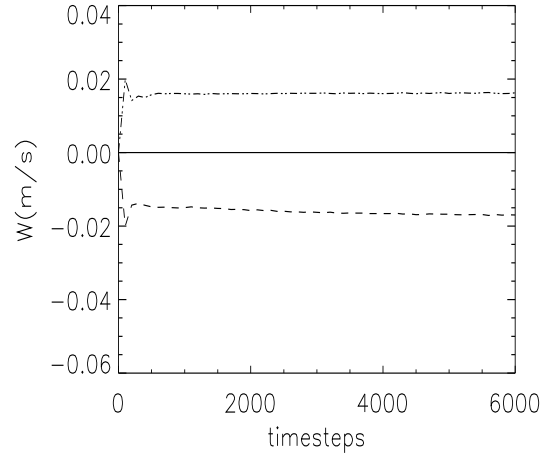
b)



e)

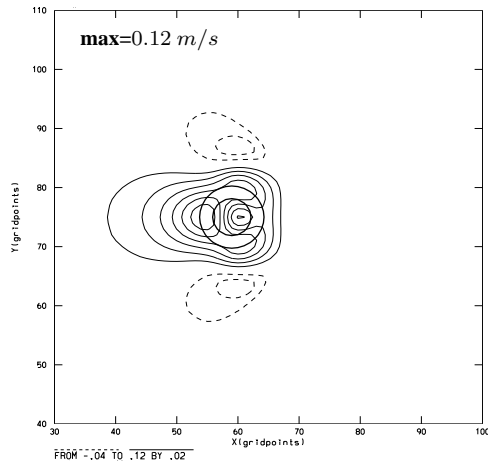


c)

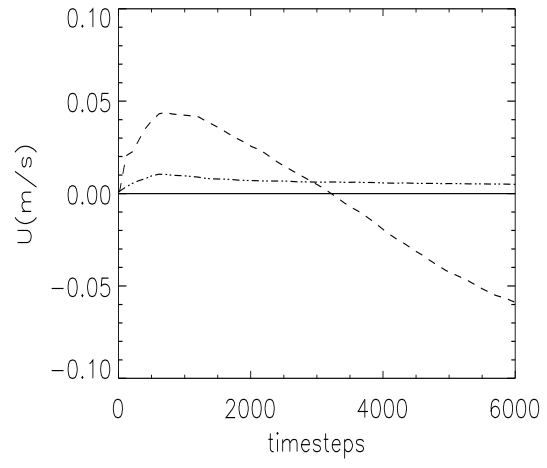


f)

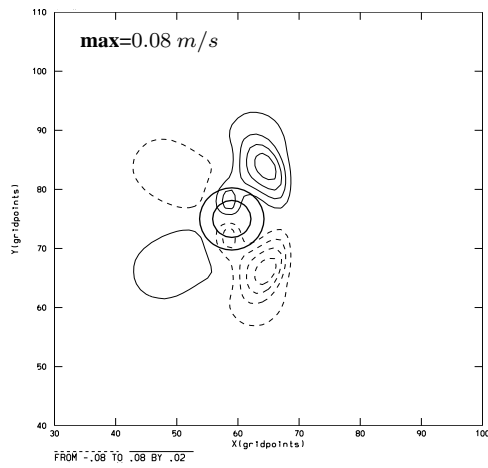
Figure 4.6: Results of Experiment 1, Run 1 with application of the *Gal-Chen* coordinate. Horizontal cross-sections of u (Panel a, cont.-int. 0.02 m/s) and v (Panel b, cont.-int. 0.02 m/s) at $z = 1800 \text{ m}$. Thick lines show $\bar{h}/3$ and $2\bar{h}/3$ contours of the topography. Vertical cross-section of vertical velocity w (Panel c, cont.-int. 0.001 m/s) at $y = 0 \text{ m}$. The horizontal dashed lines denote the shear layer of U . Positive contours are solid, negative are dashed. Right panels show maxima (dashed-dotted) and minima (dashed) of the velocity components u (Panel d), v (Panel e) and w (Panel a) versus time. The maxima and minima are computed with Eq. (4.6).



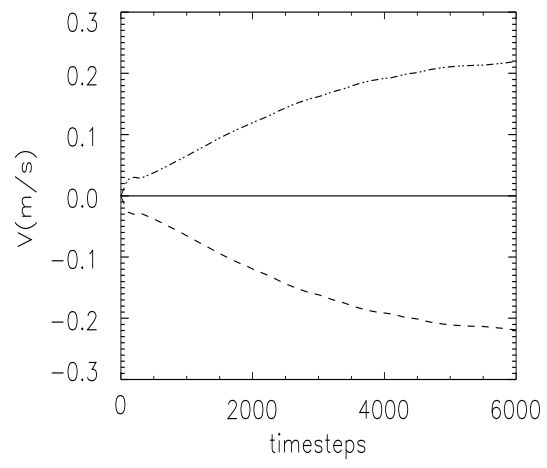
a)



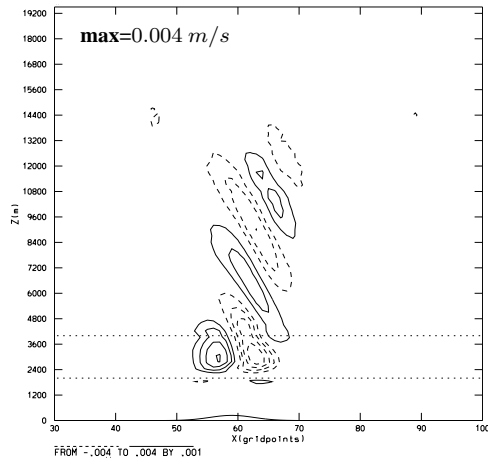
d)



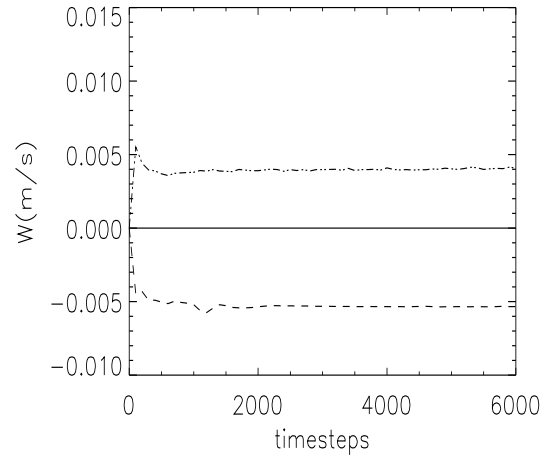
b)



e)

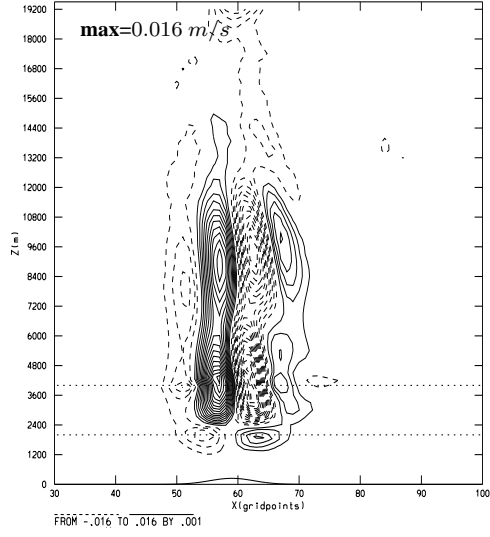


c)

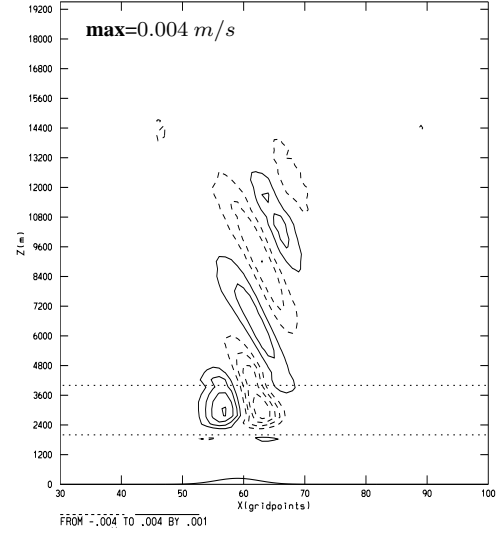


f)

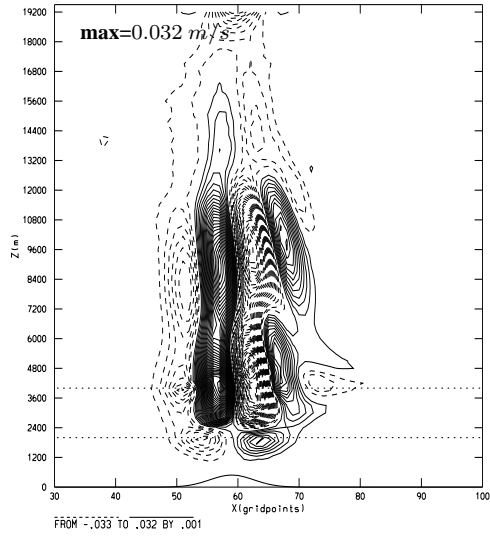
Figure 4.7: As Fig. 4.6, but computed using the new coordinate.



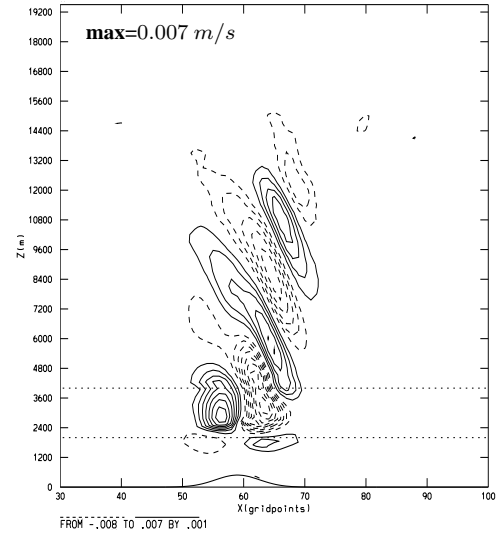
a) $\tilde{h} = 250 \text{ m}$, $a = 10 \text{ km}$



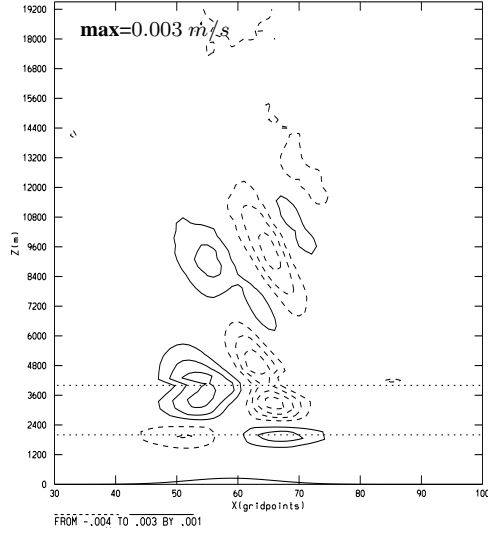
e) $\tilde{h} = 250 \text{ m}$, $a = 10 \text{ km}$



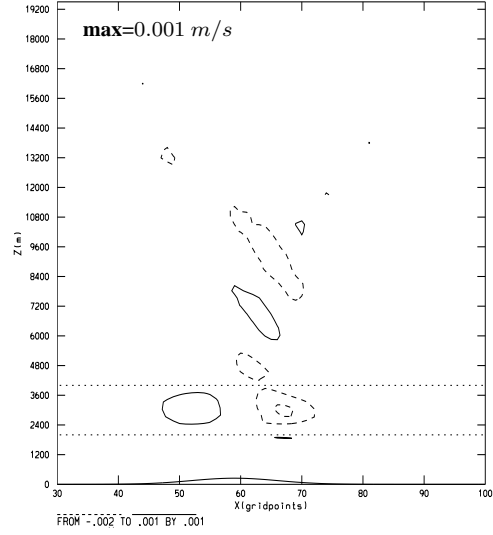
b) $\tilde{h} = 500 \text{ m}$, $a = 10 \text{ km}$



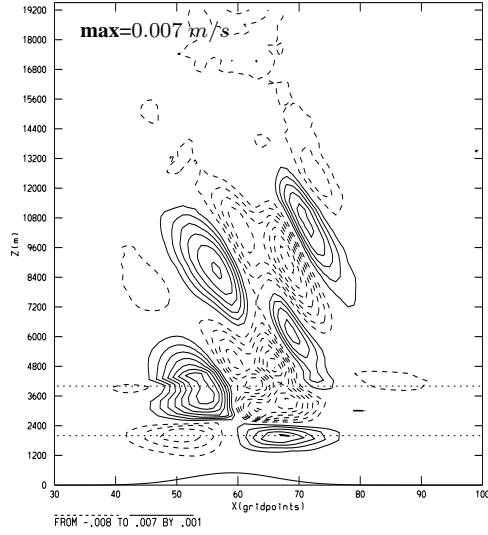
f) $\tilde{h} = 500 \text{ m}$, $a = 10 \text{ km}$



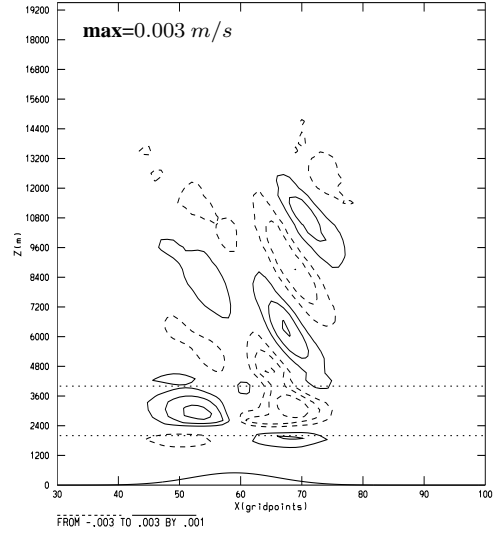
c) $\tilde{h} = 250 \text{ m}$, $a = 20 \text{ km}$



g) $\tilde{h} = 250 \text{ m}$, $a = 20 \text{ km}$



d) $\tilde{h} = 500 \text{ m}$, $a = 20 \text{ km}$



h) $\tilde{h} = 500 \text{ m}$, $a = 20 \text{ km}$

Figure 4.8: Results of Experiment 1, Runs 1-4. Vertical cross-sections of vertical velocity w at $y = 0 \text{ m}$. Left Panels a-d show runs with *Gal-Chen* coordinate, right Panels e-h show runs with new coordinate. Positive contours are solid, negative are dashed, contour interval is 0.001 m/s . The horizontally dashed lines denote the shear layer of U .

Experiment 2

In Experiment 1 the new coordinate has been applied with fixed scale-heights of $s_1 = 4000 \text{ m}$ and $s_2 = 2000 \text{ m}$ resulting in invertibility factors of $\alpha_{inv} < 0.2$, depending on the dimensions of the Gaussian hill. In a second experiment we will now vary the invertibility factor and study the effect of the transformation error on w for a Gaussian hill of $\tilde{h} = 2000 \text{ m}$ and $a = 20000 \text{ m}$. The setup is identical to Experiment 1, except that the shear layer is lifted according to the height of the hill: $z_{s_1} = 4000 \text{ m}$, $z_{s_2} = 6000 \text{ m}$. The following runs are performed:

Run 1: *Gal-Chen* coordinate

Run 2: New coordinate with $s_1 = 4230 \text{ m}$, $s_2 = 3700 \text{ m}$, thus $\alpha_{inv} = 0.5$

Run 3: New coordinate with $s_1 = 3020 \text{ m}$, $s_2 = 2640 \text{ m}$, thus $\alpha_{inv} = 0.7$

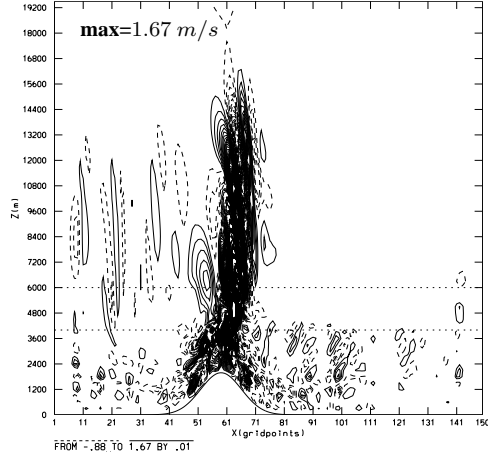
Run 4: New coordinate with $s_1 = 2350 \text{ m}$, $s_2 = 2050 \text{ m}$, thus $\alpha_{inv} = 0.9$

Run 5: New coordinate with $s_1 = 2110 \text{ m}$, $s_2 = 1850 \text{ m}$, thus $\alpha_{inv} = 1.0$

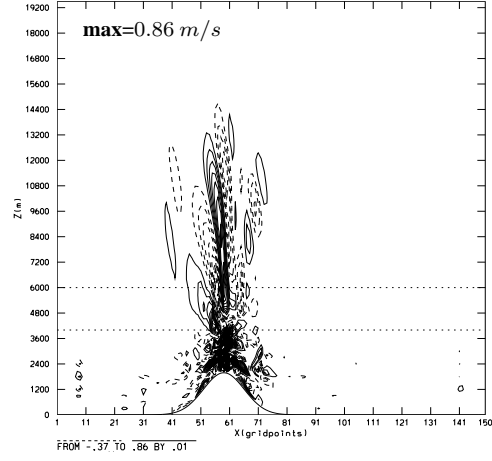
Run 6: New coordinate with $s_1 = 1410 \text{ m}$, $s_2 = 1232 \text{ m}$, thus $\alpha_{inv} = 1.5$

Note, that in Run 6 a choice of scale-heights is applied, which does *not* satisfy the invertibility condition. In Fig. 4.9 the results of Runs 1-6 are shown. The structure of the w -field differs slightly from that of Experiment 1 (c.f. Fig. 4.8). The error in w computed with the *Gal-Chen* coordinate is not restricted to areas above the mountain but is spread over the whole area of the stagnant layer and aloft, as well as upstream of the mountain (Fig. 4.9a). The reason for this difference is not known, since the only difference in the setup as compared to that of Experiment 1 is the mountain height, which is roughly eight times larger. Moreover, it has to be noted, that the flow computed in Run 1 is not in a steady state, and thus these results must be considered with care. Nevertheless, Figure 4.9b-e show that the application of the new coordinate with an increasing invertibility factor decreases the effects of the transformation error by a factor of up to 30 (!). Even an invertibility factor of $\alpha_{inv} = 1.0$ yields good results. It is worth noting that the *Gal-Chen* coordinate causes erroneous vertical winds of up to 1.7 m/s , which can have a critical impact on condensation, precipitation and convection in real atmospheric simulations. With the new coordinate, however, such errors are not observed.

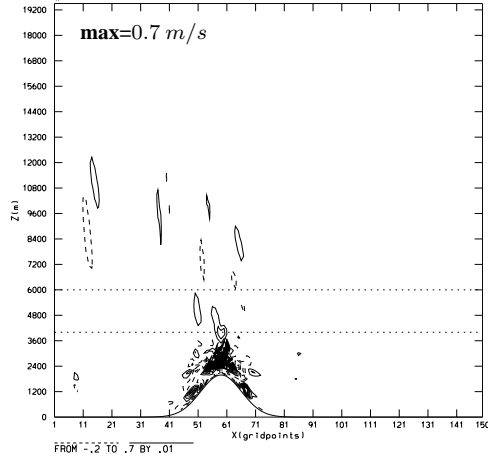
For $\alpha_{inv} = 1.5$ the invertibility condition is no longer satisfied. Near the surface the computational levels collapse and the coordinate transformation fails to yield reliable results, as can be clearly seen from Figure 4.9f.



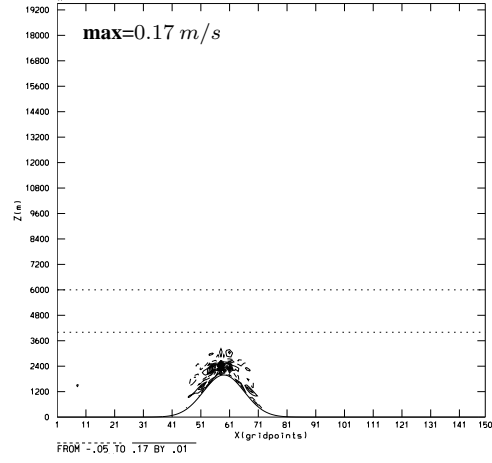
a) *Gal-Chen*



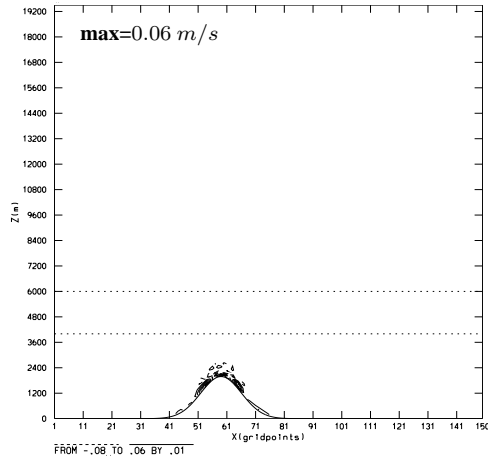
b) $\alpha_{inv} = 0.5$



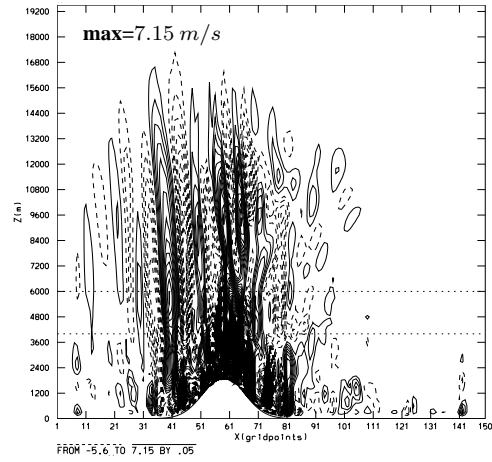
c) $\alpha_{inv} = 0.7$



d) $\alpha_{inv} = 0.9$



e) $\alpha_{inv} = 1.0$



f) $\alpha_{inv} = 1.5$

Figure 4.9: Results of Experiment 2. Vertical cross-sections of vertical velocity w at $y = 0$ m. Comparison of different vertical coordinates: *Gal-Chen* coordinate (Panel a), new coordinate with $\alpha_{inv} = 0.5$ (Panel b), $\alpha_{inv} = 0.7$ (Panel c), $\alpha_{inv} = 0.9$ (Panel d), $\alpha_{inv} = 1.0$ (Panel e) and $\alpha_{inv} = 1.5$ (Panel f). Positive contours are solid, negative are dashed, contour interval is 0.01 m/s (except for Panel f, where it is 0.05 m/s). The horizontal dashed lines denote the shear layer of U .

4.3.2 Case study 2: Uniform Flow past Complex 2D-Topography

In Case study 1 the new coordinate has only been tested in connection with smooth topography. Although a substantial decrease of the transformation error has been achieved as compared to the *Gal-Chen* coordinate, the benefit of the *scale-dependent* vertical decay of the terrain features could not be demonstrated with the smooth Gaussian hills considered so far. The two Experiments presented in this case study involve uniform flow past complex 2D-topography and aim at the comparison between the exponential coordinate and the new, scale-dependent coordinate.

Both experiments involve linear, uniformly stratified flow past a complex two dimensional topography. The flow is disturbed from its equilibrium state while forced to rise over the terrain, and mountain waves, which vertically carry away the energy associated with this disturbance, are excited ([Durrant, 1990](#)). If the frequency of the forcing, i.e. $2\pi U_0/\lambda$ (where λ is the wavelength of the topography), exceeds the eigenfrequency N of the atmosphere, the waves cannot propagate and decay exponentially with height, while for frequencies lower than N , the waves propagate vertically. The critical wavelength for the setup described below has a value of $\lambda_{crit} = 6283 \text{ m}$.

Setup

The domain under consideration is described by Eq. (2.2) and is bounded below by a complex topography similar to that used in the 2D advection study described in Chapter 3. It consists of a large-scale Gaussian-shaped envelope and a superimposed small-scale perturbation

$$h(x) = \tilde{h} \exp \left[- \left(\frac{x}{a} \right)^2 \right] \cos \left(\frac{\pi x}{\lambda_2} \right)^2, \quad (4.7)$$

where \tilde{h} denotes the height, a the halfwidth of the large-scale part and λ_2 the wavelength of the small-scale part. For convenience, we introduce an arbitrary large-scale wavelength λ_1 , which is defined as $\lambda_1 = 2\pi a$, which corresponds to a large-scale wavelength. The basic state flow is given by $U = U_0$, $V = 0 \text{ m/s}$, $\bar{w} = 0 \text{ m/s}$. Periodic boundary conditions in y -direction are applied, thus the resulting flow is quasi-twodimensional and the y -extent of the domain can be chosen small. In Table 4.2 the values of selected variables of the setup are specified.

x_{min}	-100000 m	y_{min}	-10000 m	H	19500 m
x_{max}	100000 m	y_{max}	10000 m	U_0	10 m/s

Table 4.2: Variables and corresponding values of the setup of Case study 2. For a description of the variables see Eq. (3.1)

The vertical spacing of the 65 computational levels is uniform and

$$\Delta z = \Delta \eta = \Delta Z = 300 \text{ m}.$$

The horizontal discretization is dependent on the Experiment and will later be defined.

Linear and Reference Solution

If the mountain height is sufficiently small, i.e. $\tilde{h}N/U_0 < 1$ and thus, the resulting flow is in the linear regime, a solution based on linear theory can be computed (Smith, 1980). The basic idea of this approach is to compute the Fourier transform of the topography and to determine the forcing for each Fourier mode. The result in physical space can then be obtained by an inverse transform. A FORTRAN program by Daniel Lüthi (Lüthi et al. (1989), Lüthi (1993)) has been used for the computation of a linear solution of the flows under investigation. These solutions, hereafter referred to as 'linear solutions', are computed with the same resolution as, and are used for comparison with the solutions computed with MC2.

In addition a high-resolution 'reference solution' with all three coordinates is computed for each Experiment. Experience has shown that the high-resolution reference runs do not depend on the choice of vertical coordinate, so only the results of the *Gal-Chen* coordinate are shown.

Experiment 1

A first Experiment involves uniform flow past topography with $\tilde{h} = 250 \text{ m}$, $\lambda_1 = 125664 \text{ m}$ and $\lambda_2 = 16000 \text{ m}$, therefore both parts of the topography force waves with $\lambda > \lambda_{crit}$, which do not decay vertically. The horizontal resolution is given by $\Delta x = 2000 \text{ m}$, thus the small-scale part of the topography has a wavelength of $8\Delta x$. The time step is $\Delta t = 30 \text{ s}$ and the integration time is chosen such that the flow is in a steady state to a good approximation. The following runs are performed:

Run 0: Linear solution

Run 1: *Gal-Chen* coordinate

Run 2: High-resolution run (*Gal-Chen* coordinate, $\Delta x = 500 \text{ m}$, $\Delta t = 8 \text{ s}$)

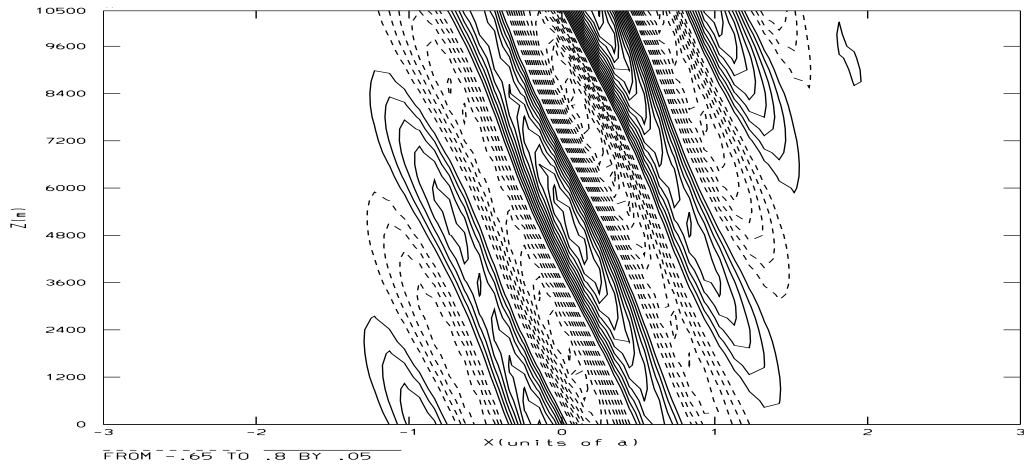
Run 3: Exponential coordinate with $s = 3000 \text{ m}$, thus $\alpha_{inv} = 0.1$

Run 4: New coordinate with $s_1 = 5000 \text{ m}$, $s_2 = 2000 \text{ m}$, thus $\alpha_{inv} = 0.1$

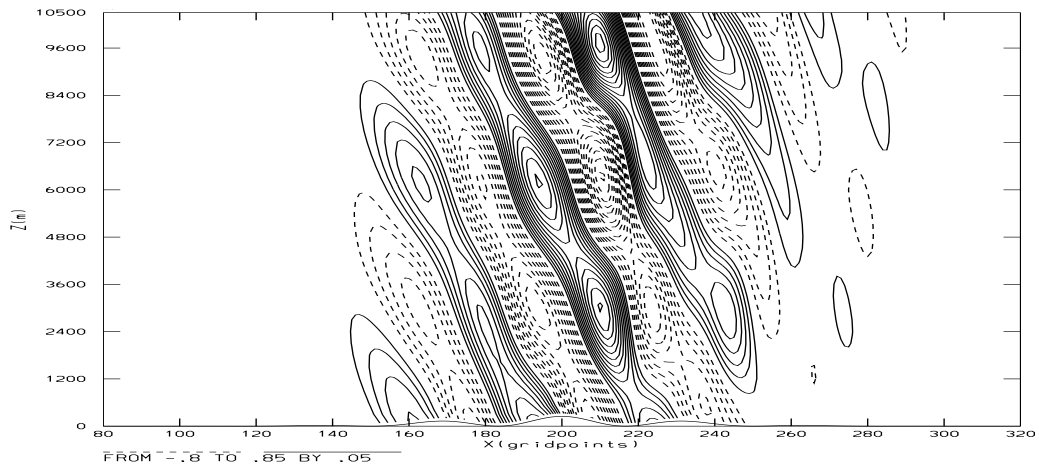
Run 5: Exponential coordinate with $s = 250 \text{ m}$, thus $\alpha_{inv} = 1.0$

Run 6: New coordinate with $s_1 = 286 \text{ m}$, $s_2 = 234 \text{ m}$, thus $\alpha_{inv} = 1.0$

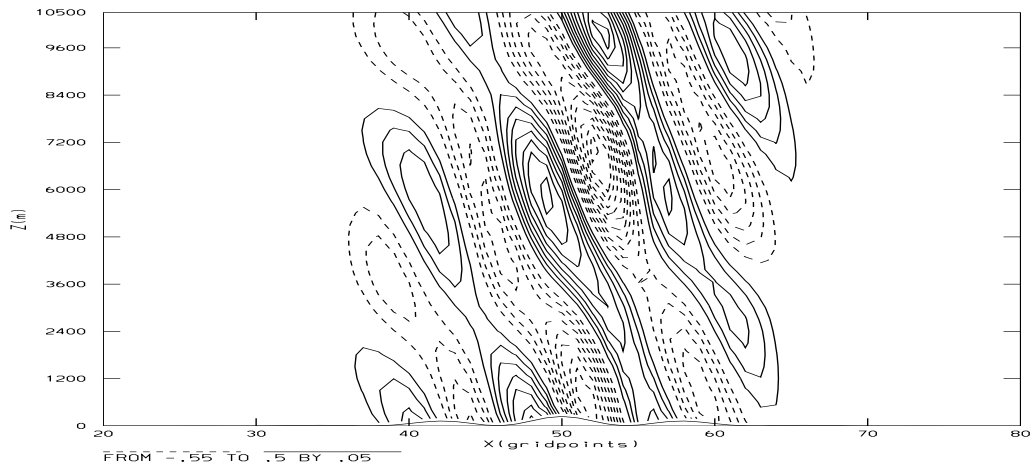
Figure 4.10 shows the results of Runs 0-4. All panels show cross-sections of the vertical velocity w at $y = 0 \text{ m}$. The linear solution (Fig. 4.10a) and the Reference solution (Fig. 4.10b) agree well both in amplitude and structure of the wave patterns. The high resolution solution shows a slightly changed distribution of the maxima in the amplitude, as compared to the linear solution, which is likely to have its origin in reflections at the upper nesting sponge, of which the lower boundary is located at $z = 10500 \text{ m}$.



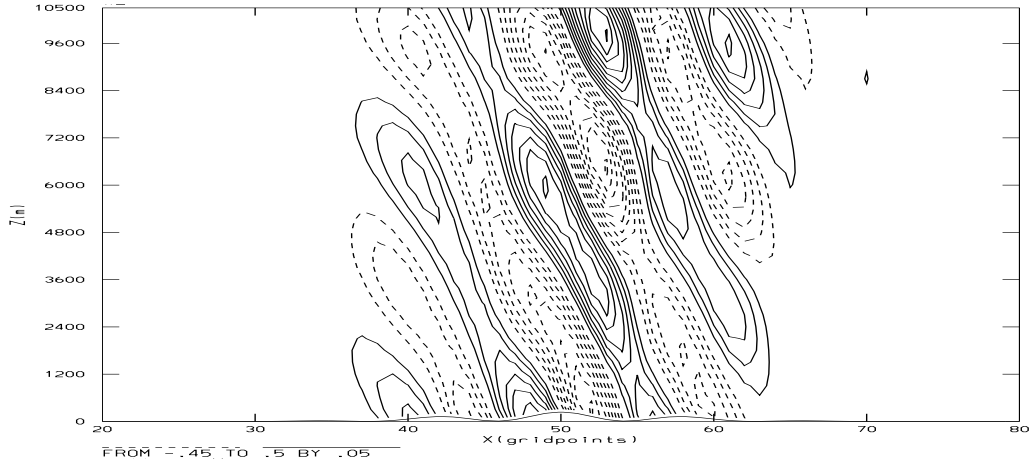
a) Linear solution



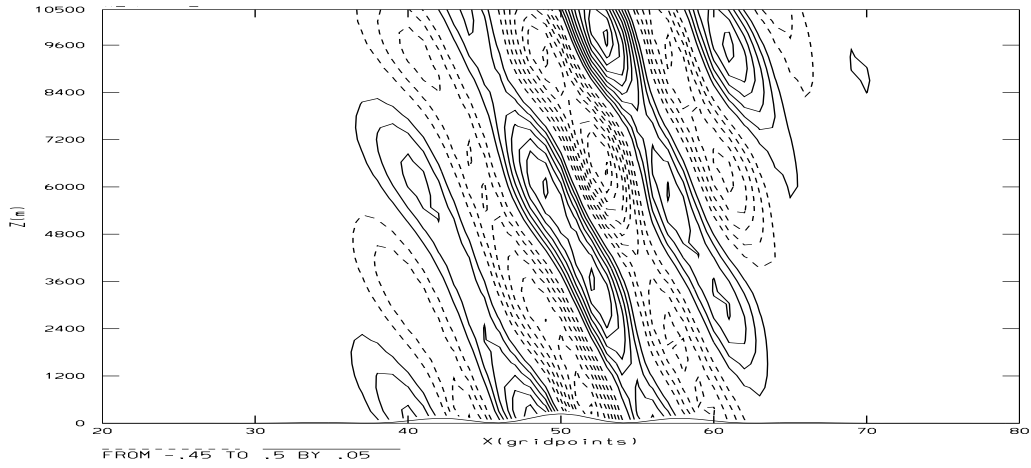
b) Reference solution



c) Gal-Chen coordinate

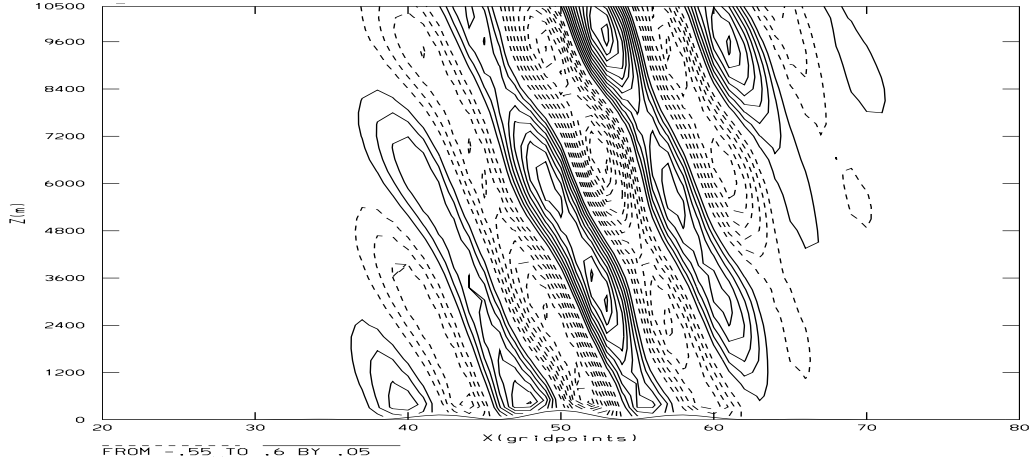


d) Exponential coordinate

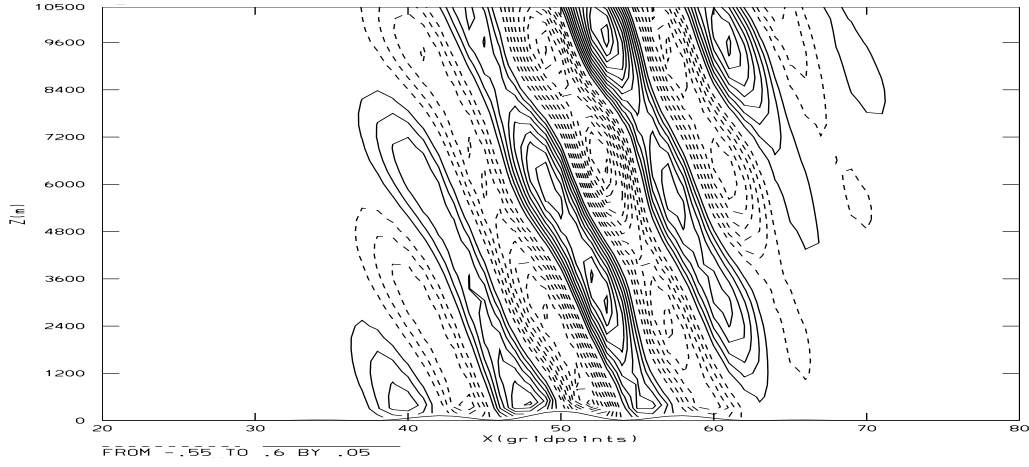


e) New coordinate

Figure 4.10: Results of Experiment 1, Runs 0-4. Vertical cross-sections of vertical velocity w at $y = 0$ m. Linear solution (Panel a), high-resolution solution (Panel b), solutions with *Gal-Chen* coordinate (Panel c), exponential coordinate (Panel d) and new coordinate (Panel e). Positive contours are solid, negative are dashed, contour interval is 0.05 m/s.



a) Exponential coordinate, $\alpha_{inv} = 1.0$



b) New coordinate, $\alpha_{inv} = 1.0$

Figure 4.11: Results of Experiment 1, Runs 5 and 6. As Fig. 4.10, but with application of the exponential coordinate (Panel a) and new coordinate (Panel b) with an invertibility factor of $\alpha_{inv} = 1.0$

The solutions with the *Gal-Chen* coordinate (Fig. 4.10c), the exponential coordinate (Fig. 4.10d) and the new coordinate (Fig. 4.10e) all show approximately the same loss in amplitude as compared to the reference solution. This loss in amplitude is assumed to be caused by implicit numerical diffusion, which is more pronounced for poorly resolved flow features (c.f. Appendix). The *Gal-Chen* solution features a considerable error in the wave-structure, which is likely to be caused by transformation errors. It is worth noting, that the difference between the exponential and the new coordinate is only minor. In Fig. 4.11 the results of the runs with an invertibility factor of $\alpha_{inv} = 1.0$ are shown. Differences are apparent if one compares these results with those of Figure 4.11d,e: The amplitude of the waves is reproduced slightly better in higher regions with $\alpha_{inv} = 1.0$. However, the large vertical gradients at the surface possibly indicate the limitation of the use of a coordinate transformation with a critical invertibility factor. Thus, care should be taken with a choice of α_{inv} close to unity.

Experiment 2

A second experiment is performed, which is identical to Experiment 1, except that a topography with a small-scale wavelength of $\lambda_2 = 12000 \text{ m} = 6\Delta x$ is used. All runs show, that the poor resolution of the flow features causes considerable errors both in amplitude and structure of the wave patterns. The *Gal-Chen* coordinate completely fails to reproduce the expected flow structure, but also the results achieved with the exponential and the new coordinate indicate that with this spacial resolution of the topography and this setup of the model, such small scale mountain waves cannot be accurately simulated. The figures with results of Experiment 2 can be found in [Appendix \(A.1\)](#)

Experiment 3

The third Experiment differs in the type of mountain waves generated by the topography from the Experiments described before. In the first two Experiments both the large-scale and the small-scale part of the terrain force hydrostatic waves, i.e. the induced mountain wave amplitude does not decay with height. The topography used in Experiment 3 is given by $\tilde{h} = 250 \text{ m}$, $\lambda_1 = 31415 \text{ m}$ and $\lambda_2 = 4000 \text{ m}$, thus the two different scales of the topography force different types of waves. The waves generated by the large-scale part are hydrostatic, i.e. they do not decay with height, while the waves forced by the small-scale part are non-hydrostatic, i.e. they decay exponentially with height. According to [Durrant \(1990\)](#) the scale-height of decay is determined by

$$\mu^{-1} = \sqrt{(2\pi/\lambda_2)^2 - (N/U_0)^2} = 826 \text{ m}, \quad (4.8)$$

thus at heights $z > 3000 \text{ m}$ the small-scale features of the wave patterns are damped by a factor of at least 98%, while the large-scale features are not damped. (c.f. [Fig. 4.12](#))

The horizontal resolution is given by $\Delta x = 500 \text{ m}$, thus the small-scale part has a wavelength of $8\Delta x$. The time step is $\Delta t = 8 \text{ s}$ and the integration time is chosen in a way, that the flow is in a steady state to a good approximation. The following runs are performed:

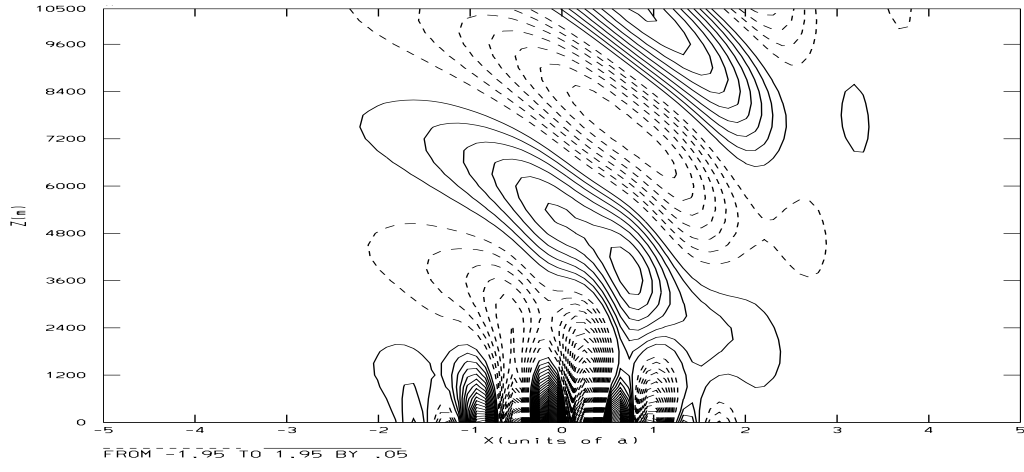
Run 0: Linear solution

Run 1: *Gal-Chen* coordinate

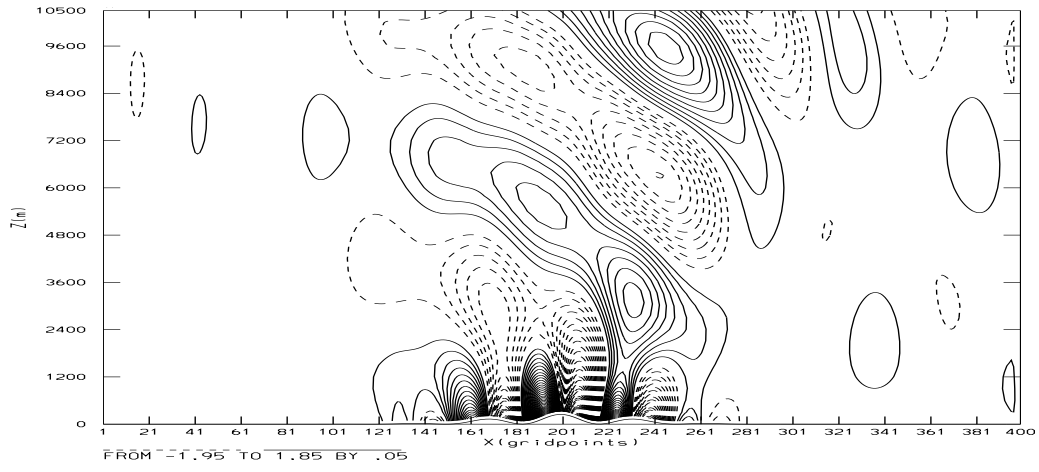
Run 2: High-resolution run (*Gal-Chen* coordinate, $\Delta x = 125 \text{ m}$, $\Delta t = 2 \text{ s}$)

Run 3: Exponential coordinate with $s = 3000 \text{ m}$, thus $\alpha_{inv} = 0.1$

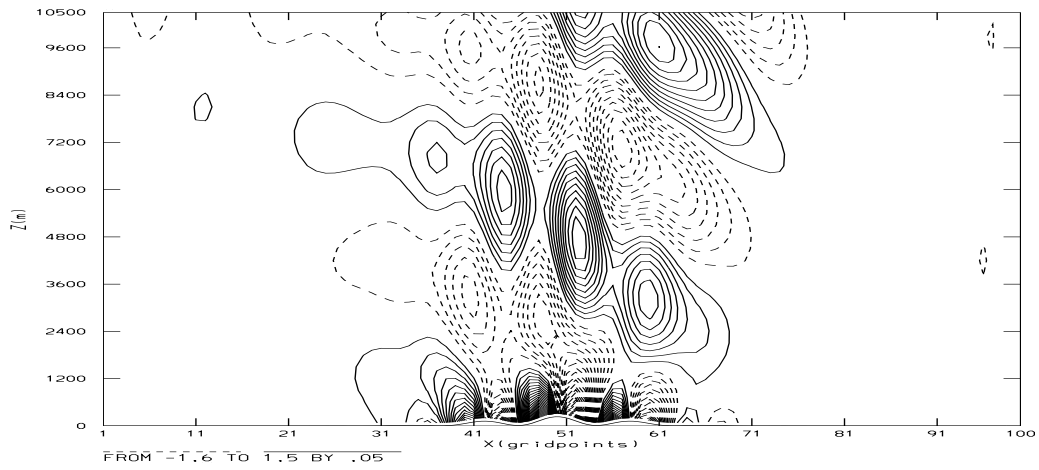
Run 4: New coordinate with $s_1 = 5000 \text{ m}$, $s_2 = 2000 \text{ m}$, thus $\alpha_{inv} = 0.1$



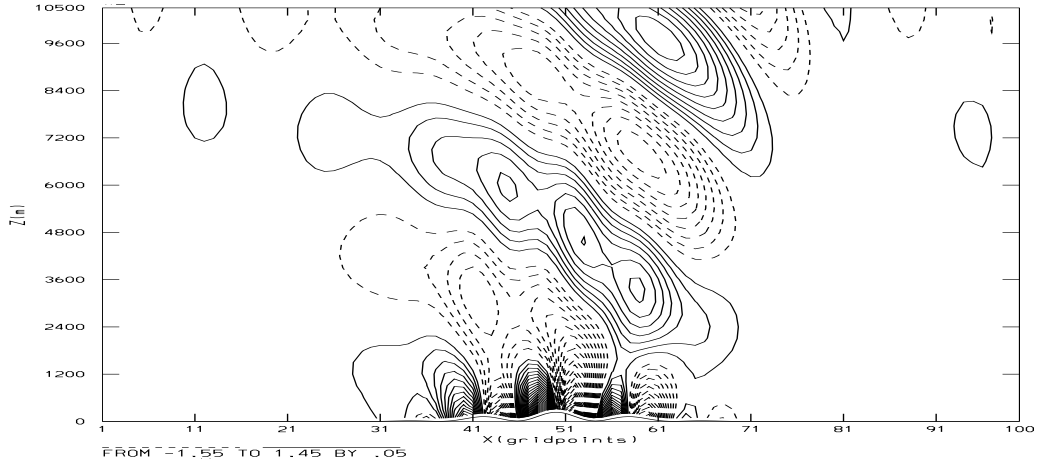
a) Linear solution



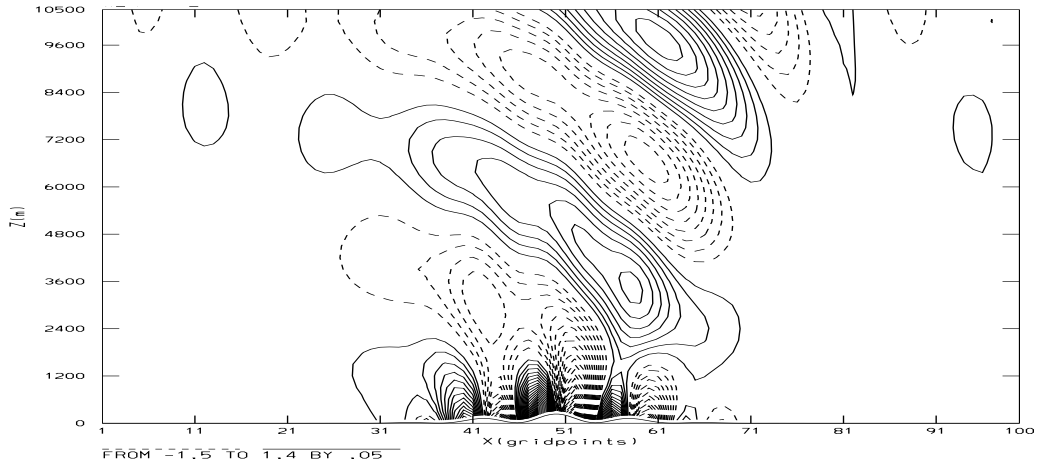
b) Reference solution



c) Gal-Chen coordinate



d) Exponential coordinate



e) New coordinate

Figure 4.12: Results of Experiment 3, Runs 0-4. Vertical cross-sections of vertical velocity w at $y = 0$ m. Linear solution (Panel a), high-resolution solution (Panel b), solutions with *Gal-Chen* coordinate (Panel c), exponential coordinate (Panel d) and new coordinate (Panel e). Positive contours are solid, negative are dashed, contour interval is 0.05 m/s.

Fig. 4.12 shows the results of Runs 0-4. All panels show cross-sections of the vertical velocity w at $y = 0$ m. The reflections at the upper sponge in the high-resolution solution (Fig. 4.12b) are more pronounced as compared to those of Experiment 1. This might be explained by the fact, that in Experiment 3 the timestep is reduced by a factor of four, while the integration time is unchanged, thus the nesting applied in every time has a much stronger effect on the computed solution. A weaker nesting parameter would probably decrease the amount of reflection. Since this effect is the same for all three coordinates, the comparison of the coordinates is not affected. The solution computed with the *Gal-Chen* coordinate (Fig. 4.12c) completely fails to accurately reproduce the large-scale wave structure of the flow. Small-scale features in the large-scale wave patterns are clearly visible up to a height of 10000 m and relative deviations in amplitude from the reference solution reach values of up to 60%, which are very likely to be caused by a transformation error for two reasons: Firstly, as noted above, all small-scale wave patterns are physically damped with height and secondly the linear solution (Fig. 4.12a) and the solutions with the exponential (Fig. 4.12d) and new coordinate (Fig. 4.12e) do not show this error. It is worth noting that the solution computed with the new coordinate shows an excellent agreement with the linear solution in both, amplitude and structure. The solution with the exponential coordinate, however, features similar but less pronounced small-scale features in the large-scale wave structure as are obtained with the *Gal-Chen* coordinate. The main difference between these two coordinates is expected to be seen at heights between 2000 m and 6000 m, because the difference in the computational level-heights of the two coordinates are most pronounced in this region. A comparison of Fig. 4.12d and Fig. 4.12e confirms this assumption.

Experiment 4

A fourth Experiment is performed, which is identical to Experiment 3, except that a topography with a small-scale wavelength of $\lambda_2 = 3000$ m = $6\Delta x$ is used. The results are comparable to that of Experiment 3 and confirm the good results of the new coordinate obtained in Experiment 3. The figures with results of Experiment 4 can be found in Appendix (A.2)

Chapter 5

Conclusion and Outlook

In this chapter the results obtained with the 2D advection study described in *Chapter 3* and those of the two Case studies with MC2, described in *Chapter 4* are briefly rehashed and discussed. In a second part, proposals for a continuation of this work are outlined.

Stagnant Layer over Complex Topography

Both the 2D advection study (described in *Chapter 3*) and Case study 1 (described in *Section 4.3.1*) involve horizontal flow without interaction with the underlying topography. In both cases the *Gal-Chen* coordinate generates serious transformation errors in the computed fields. In a model using full dynamics, this error can propagate to regions away from the source. Moreover, it has been observed that the transformation can cause unphysical flow features like considerable errors in the vertical velocity. This could have a considerable impact on processes such as condensation, precipitation and convection-triggering for real-case simulations, and thus, introduce significant errors in the simulated fields. It has been shown that both the exponential and the new coordinate can considerably (up to an order of magnitude) reduce this error, as compared to the *Gal-Chen* coordinate.

The aforementioned effect is more pronounced for topographies of small resolution. For smooth topographies the performance of the exponential and the new coordinate are comparable. If the scale-heights s_1 and s_2 are decreased, i.e. for an increasing invertibility factor, the transformation error can be further reduced. Thus a coordinate transformation featuring a fast transition to smooth levels is favorable for this type of flow, which is best accomplished with the application of the new, non-local coordinate. However, care has to be taken with the choice of the scale heights. A choice of the invertibility factor exceeding unity leads to the collapse of the near-surface computational levels and thus to large errors in the computed flow field.

Forcing of both Non-Hydrostatic and Hydrostatic Mountain Waves by Complex Topography

The resulting flow of Experiment 3 and 4 of Case study 2 (described in Section 4.3.2) is a superposition of two wave-components: A hydrostatic component of the wave, forced by the large-scale part of the topography, which does not decay with height, forms large-scale flow features and propagates vertically. On the other hand, non-hydrostatic waves are forced by the small-scale part of the topography, which decay exponentially with height. Thus, at upper levels, the flow is decoupled of the fine-scale topography structure. Again, the *Gal-Chen* coordinate is not capable of representing the large-scale flow patterns correctly and gives relative errors in w up to 60%. Solutions computed with this coordinate exhibit considerable small-scale terrain features in regions, where only large-scale patterns can be of physical origin. The same effect, even though less pronounced, is also obvious in the solution computed with the exponential coordinate. With the new coordinate, however, results are obtained, which show a good agreement with both the linear and the reference solution. The small-scale errors visible in the large-scale patterns can be almost completely removed. This clearly demonstrates the advantage of a scale-dependent coordinate, which allows for the fast vertical decay of small-scale terrain features.

Forcing of pure Hydrostatic Mountain Waves by Complex Topography

For the pure hydrostatic wave-like flow described in Experiment 1 and 2 of Case study 2 the flow features structures of the same horizontal scale as the underlying topography throughout the whole vertical extent of the domain. The benefit of the exponential and the new coordinate for this flow, which is strongly coupled to the underlying terrain, is found to be comparatively minor. Results obtained with both the exponential and new coordinate with an invertibility factor of unity show, that large vertical gradients appear in near-surface regions of the flow fields. Thus in order to obtain reliable results, a choice of the scale-heights resulting in an invertibility factor of less than unity is strongly recommended.

In this study we have successfully implemented the new, scale-dependent coordinate into the non-hydrostatic NWP model MC2 and have shown that this formulation performs well, when applied to full dynamics and three dimensions. The computational overhead and the enhanced memory requirements for the storage of the fully threedimensional metric terms is found to be comparatively minor. Therefore we interpret this approach as a success and recommend it for application.

Possible future research

Due to the limited scope of this study, there are many interesting topics, which could not have been treated and should be considered as a possible continuation of this work:

- It is not clear, how the new coordinate performs when physical parametrizations are included in the MC2 Model. It would be an interesting task to compute real case simulations with the new coordinate and to compare the results with those obtained with the *Gal-Chen* coordinate. During the field phase of the Mesoscale Alpine Programme (MAP) (September to November 1999) the MC2 Model was run in an operational mode. The recomputation of such runs with the new coordinate could be used for comparison and for evaluating the performance of the coordinates in real case applications.
- In this study the vertical spacing of the computational levels was always chosen uniformly. The generalized formulation of the vertical coordinate in MC2, however, allows for an unequally spacing of the levels. The investigation of the performance of the new coordinate with nonuniformly spaced levels could be part of future work.
- As described in [Section 4.2.1](#) the impact of a more sophisticated digital filter for the splitting of the topography in a small-scale part and a large-scale part on the behaviour of the coordinate could be investigated.
- As described in [Section 4.2.2](#) the metric terms of the new coordinate in MC2 could be partly evaluated analytically. The evaluation of the impact on the transformation error could be a future task.

References

- Arakawa, A., Computational design of the basic dynamical processes of the UCLA general circulation model, *Methods in Computational Physics*, 17, 173–265, 1977.
- Asselin, R. A., Frequency filter for time integrations, *Monthly Weather Review*, 100, 487–490, 1972.
- Benoit, R., M. Desgagne, P. Pellerin, S. Pellerin, Y. Chartier, and S. Desjardins, The Canadian MC2; A semi-Lagrangian, semi-implicit wide-band atmospheric model suited for fine-scale process studies and simulation, *Monthly Weather Review*, 125, 2382–2415, 1997.
- Benoit, R., et al., The real-time ultrafinescale forecast support during the special observing period of the MAP, *Bull. Amer. Meteor. Soc.*, 2002, submitted.
- Bergeron, G., R. Laprise, and D. Caya, Formulation of the mesoscale compressible community (MC2) model, *Tech. rep.*, Sciences de l’atmosphère, Département de physique, UQUAM, 1994.
- Davies, H. C., A lateral boundary formulation for multi-level prediction models, *Quart. J. Roy. Meteor. Soc.*, 102, 405–418, 1976.
- Durran, D. R., Atmospheric processes over complex terrain, *Meteorological Monographs*, 23, 59–81, 1990.
- Gal-Chen, T., and C. J. Sommerville, On the use of a coordinate transformation for the solution of the Navier-Stokes equations, *Journal of Computational Physics*, 17, 209–228, 1975.
- Lüthi, D., Mesoskalige diabatische und orographische Anregung atmosphärischer Strömungen: Theoretische Untersuchungen und numerische Simulationen, Ph.D. thesis, ETH Zürich, 1993.
- Lüthi, D., C. Schär, and H. C. Davies, Response to steady mesoscale low-level diabatic heating, *Contr. Atmos. Phys.*, 62, 126–150, 1989.
- Phillips, N. A., A coordinate system having some special advantages for numerical forecasting, *Journal of Meteorology*, 14, 184–185, 1957.
- Raymond, W. H., High-order low-pass implicit tangent filters for use in finite area calculations, *Monthly Weather Review*, 116, 2132–2141, 1988.
- Schär, C., A generalized vertical coordinate for high-resolution NWP models, pp. 1–5, 2000a.
- Schär, C., A new terrain-following vertical coordinate suited for high-resolution prediction models over complex topography, *MAP Newsletter*, 13, 1–2, 2000b.

- Simmons, A. J., and D. M. Burridge, An energy and angular-momentum conserving vertical finite-difference scheme and hybrid vertical coordinates, *Monthly Weather Review*, 109, 758–766, 1981.
- Smith, R. B., Linear theory of stratified hydrostatic flow past an isolated mountain, *Tellus*, 32, 348–364, 1980.
- Tanguay, M., A. Robert, and R. Laprise, A semi-implicit semi-Lagrangian fully compressible regional forecast model, *Monthly Weather Review*, 118, 1970–1980, 1990.
- Thomas, S. J., C. Girard, R. Benoit, M. Desgagne, and P. Pellerin, A new adiabatic kernel for the MC2 model, *Atmosphere-Ocean*, 36, 241–270, 1998.

Nomenclature

Latin Symbols

Symbol	Unit	Description
a	m	Mountain halfwidth
$a(\eta)$	m	Height of the computational level η in absence of topography
A		Arbitrary scalar field variable
$b(\eta), b_1(\eta), b_2(\eta)$	1	Vertical decay function of the terrain-following coordinate. Governs the decay of the full, large-scale and small-scale part of the topography, respectively
F		Digital filter operator
F_1, F_2	m^{-1}	Metric terms
g	ms^{-2}	Gravitational acceleration
$G_0, G_1, G_2, G^{13}, G^{23}$	1	Metric terms
h, h_1, h_2	m	Height of the full, large-scale and small-scale part of the topography, respectively
$\tilde{h}, \tilde{h}_1, \tilde{h}_2$	m	Amplitude of the full, large-scale and small-scale part of the topography, respectively
H	m	Height of model domain
H_1	m	Arbitrary height
J	1	Determinant of Jacobian matrix of the coordinate transformation
L	m	Horizontal model domain extent
M	$g\ kg^{-1}$	Water vapour content
N	s^{-1}	Brunt-Väisälä frequency
N_i, N_j, N_k	1	Number of gridpoints in x - and y -direction and number of computational levels, respectively
p, p_0	Pa	Air pressure and its value at the surface
r		Placeholder for an arbitrary variable
s, s_1, s_2	m	Rate of decay for the full, large-scale and small-scale part of the topography in the terrain-following coordinate
t	s	Time
T, T_0	K	Air temperature and its value at the surface

Symbol	Unit	Description
u, U	ms^{-1}	Velocity component in x -direction and its basic state
v, V	ms^{-1}	Velocity component in y -direction and its basic state
w, \bar{w}, w_s	ms^{-1}	Vertical velocity component, its basic state and its value at the surface, respectively
W	ms^{-1}	Vertical velocity component in terrain-following coordinates
x	m	First Cartesian coordinate
x_{min}, x_{max}	m	Limits of the model domain in x -direction
y	m	Second Cartesian coordinate
y_{min}, y_{max}	m	Limits of the model domain in y -direction
z	m	Third Cartesian coordinate
z_{lev}	m	Physical height of the computational level η
z_{s1}, z_{s2}	m	Lower and upper limit of the shear layer
Z	m	Generalized vertical terrain-following coordinate

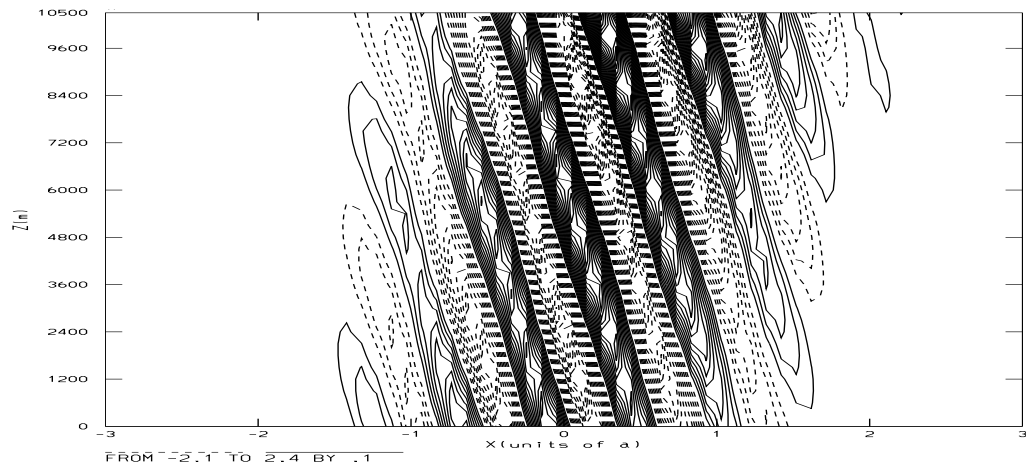
Greek Symbols

Symbol	Unit	Description
$\alpha_{inv}, \alpha_{1,inv}, \alpha_{2,inv}$	1	Invertibility factor and its scale-dependent components
η	m	Terrain-following coordinate
θ	K	Potential temperature
ϕ	1	Passive tracer variable
μ	m^{-1}	Inverse scale height of vertical decay of mountain waves
$\lambda, \lambda_1, \lambda_2$	m	Wavelength of full, large-scale and small-scale part of the topography, respectively
ν	1	Number of applications of the digital filter

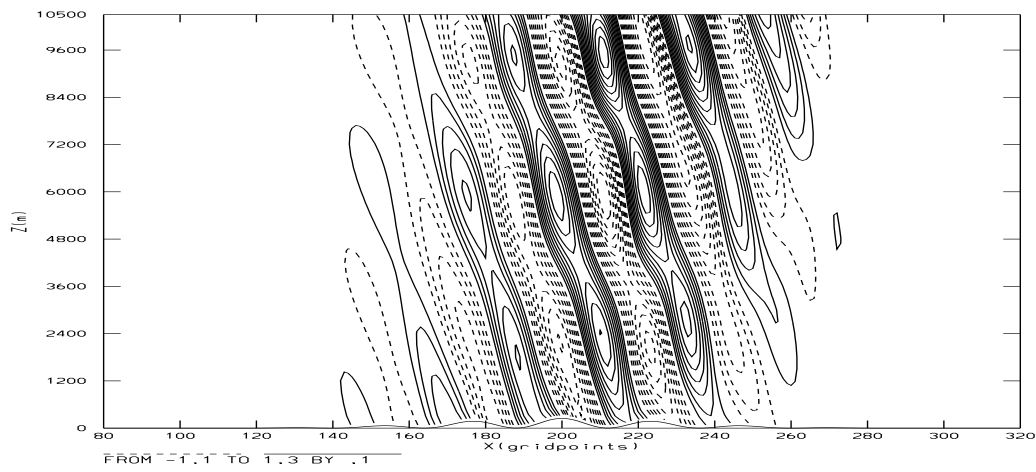
Appendix A

Selected Experiment Results

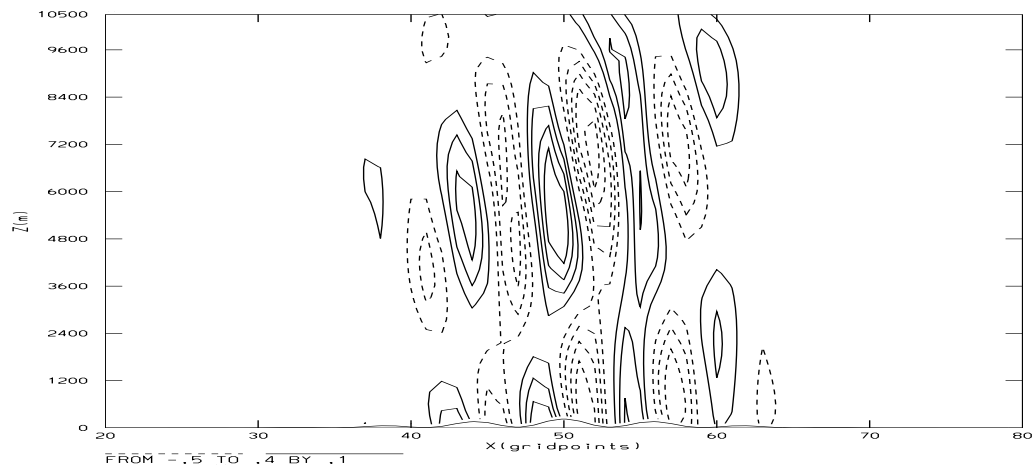
A.1 Case study 2, Experiment 2



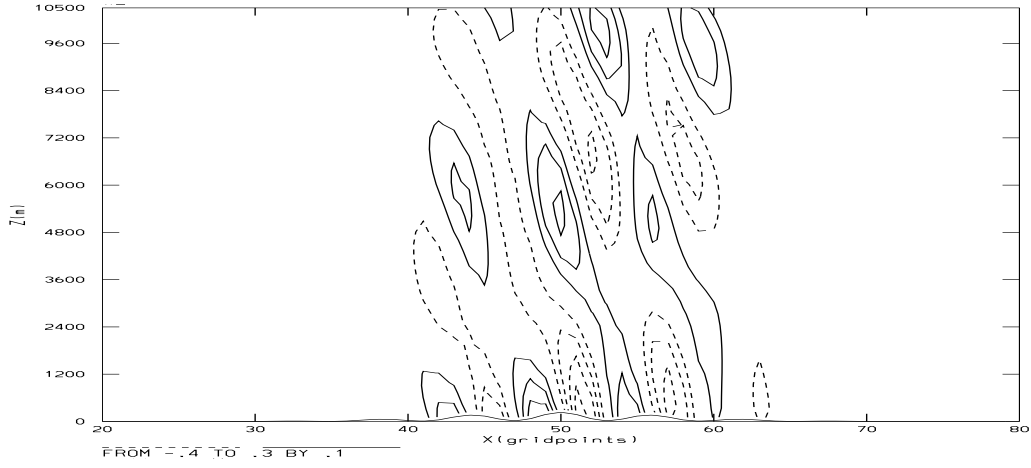
a) Linear solution



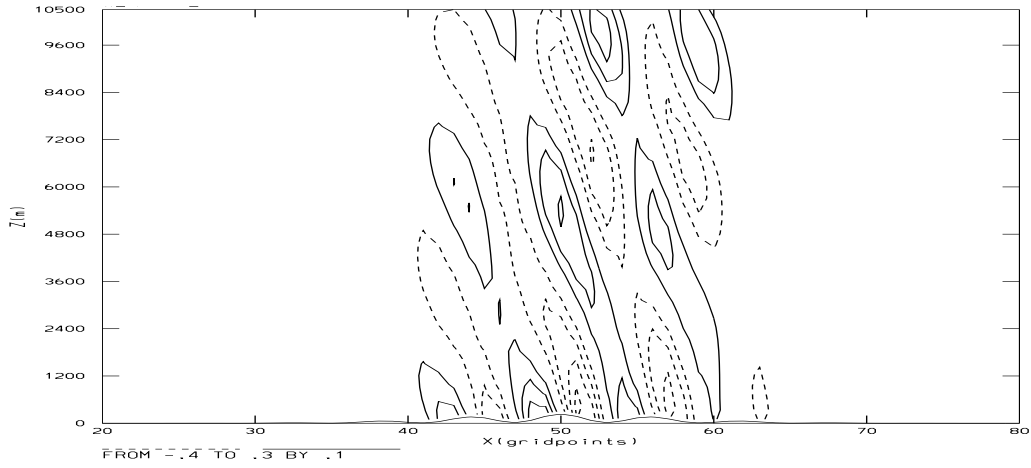
b) Reference solution



c) Gal-Chen coordinate



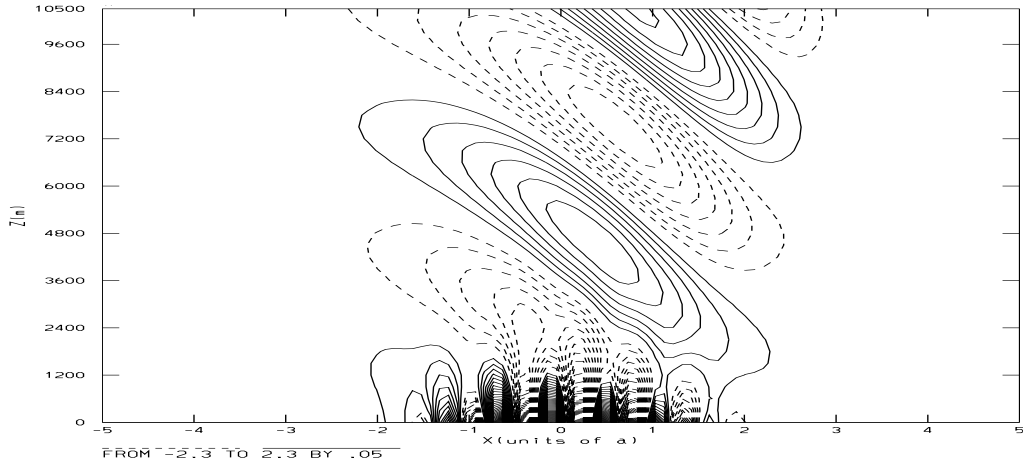
d) Exponential coordinate



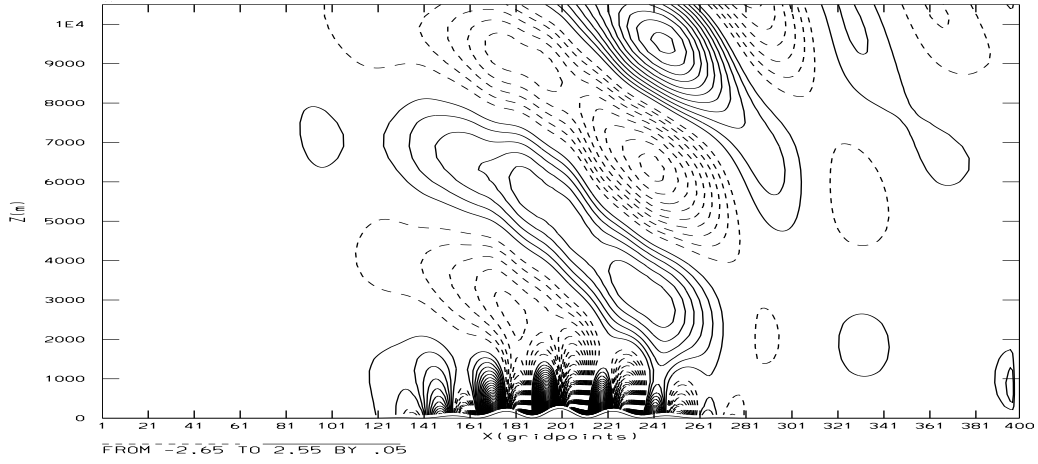
e) New coordinate

Figure A.1: Results of case study 2, Experiment 2, Runs 0-4. Vertical cross-sections of vertical velocity w at $y = 0$. Linear solution (Panel a), high-resolution solution (Panel b), solutions with *Gal-Chen* coordinate (Panel c), exponential coordinate (Panel d) and new coordinate (Panel e). Positive contours are solid, negative are dashed, contour interval is 0.1 m/s .

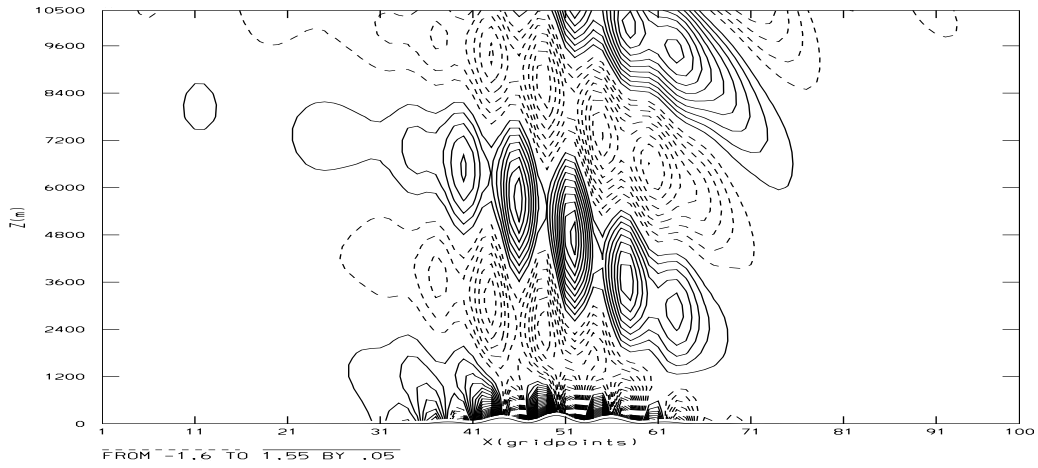
A.2 Case study 2, Experiment 4



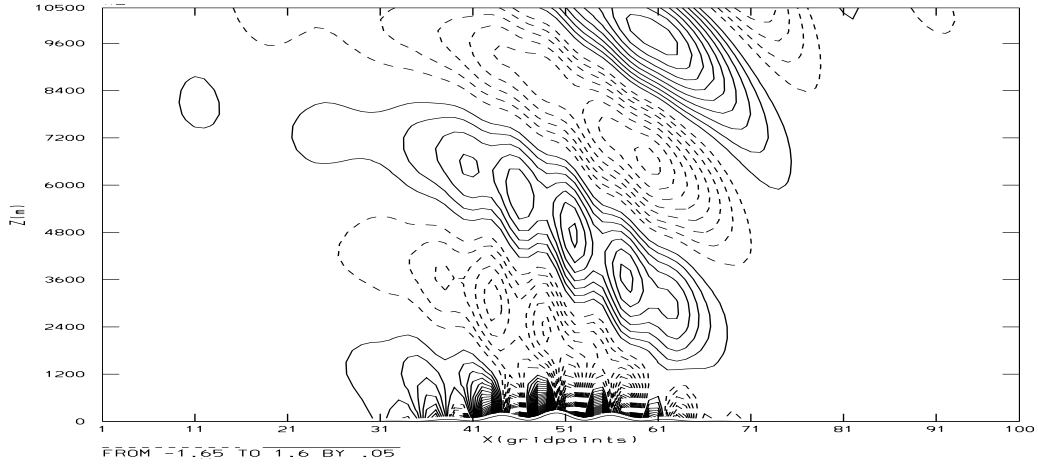
a) Linear solution



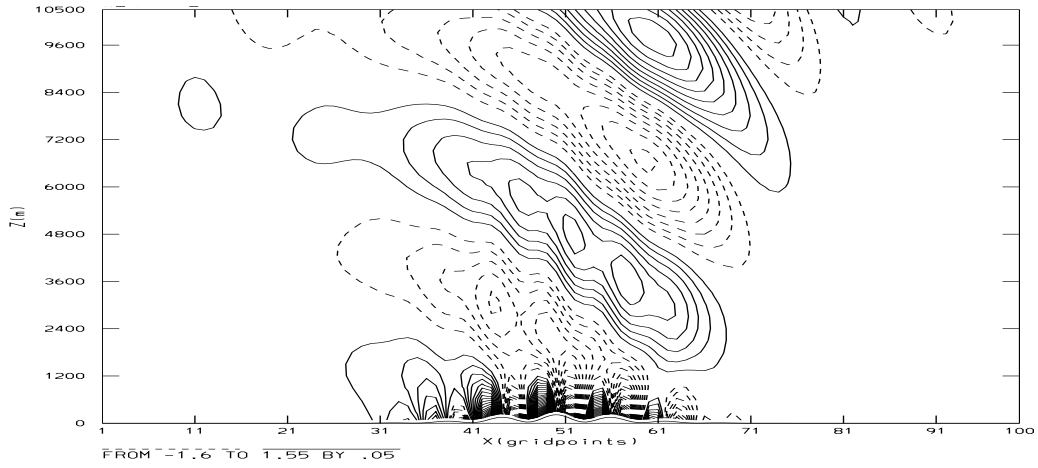
b) Reference solution



c) Gal-Chen coordinate



d) Exponential coordinate



e) New coordinate

Figure A.2: Results of Experiment 4, Runs 0-4. Vertical cross-sections of vertical velocity w at $y = 0$. Linear solution (Panel a), high-resolution solution (Panel b), solutions with *Gal-Chen* coordinate (Panel c), exponential coordinate (Panel d) and new coordinate (Panel e). Positive contours are solid, negative are dashed, contour interval is 0.05 m/s .

